Available online at www.sciencedirect.com
ScienceDirect
Applied Geochemistry 23 (2008) 1634–1659
Applied Geochemistry
www.elsevier.com/locate/apgeochem

Experimental investigations of the reaction path in the $MgO–CO_2–H_2O$ system in solutions with various ionic strengths, and their applications to nuclear waste isolation

Yongliang Xiong *, Anna Snider Lord

Sandia National Laboratories, Carlsbad Programs Group, 4100 National Parks Highway, Carlsbad, NM 88220, USA[1]

Received 26 June 2007; accepted 25 December 2007
Editorial handling by Z. Cetiner
Available online 9 February 2008

Abstract

The reaction path in the $MgO–CO_2–H_2O$ system at ambient temperatures and atmospheric CO_2 partial pressure(s), especially in high-ionic-strength brines, is of both geological interest and practical significance. Its practical importance lies mainly in the field of nuclear waste isolation. In the USA, industrial-grade MgO, consisting mainly of the mineral periclase, is the only engineered barrier certified by the Environmental Protection Agency (EPA) for emplacement in the Waste Isolation Pilot Plant (WIPP) for defense-related transuranic waste. The German Asse repository will employ a $Mg(OH)_2$-based engineered barrier consisting mainly of the mineral brucite. Therefore, the reaction of periclase or brucite with carbonated brines with high-ionic-strength is an important process likely to occur in nuclear waste repositories in salt formations where bulk MgO or $Mg(OH)_2$ will be employed as an engineered barrier. The reaction path in the system $MgO–CO_2–H_2O$ in solutions with a wide range of ionic strengths was investigated experimentally in this study. The experimental results at ambient laboratory temperature and ambient laboratory atmospheric CO_2 partial pressure demonstrate that hydromagnesite (5424) ($Mg_5(CO_3)_4(OH)_2 \cdot 4H_2O$) forms during the carbonation of brucite in a series of solutions with different ionic strengths. In Na–Mg–Cl-dominated brines such as Generic Weep Brine (GWB), a synthetic WIPP Salado Formation brine, Mg chloride hydroxide hydrate ($Mg_3(OH)_5Cl \cdot 4H_2O$) also forms in addition to hydromagnesite (5424).

The observation of nesquehonite ($MgCO_3 \cdot H_2O$) and subsequent appearance of hydromagnesite (5424) in the experiments in a Na–Cl-dominated brine (ERDA-6) at room temperature and $P_{CO_2} = 5 \times 10^{-2}$ atm allows estimation of the equilibrium constant ($\log K$) for the following reaction:

$$Mg_5(CO_3)_4(OH)_2 \cdot 4H_2O + CO_2(g) + 10H_2O = 5MgCO_3 \cdot 3H_2O$$

as ~2.5 at 25 °C. The $\log K$ for the above reaction at 5 °C is calculated to be ~4.0 by using the Van't Hoff equation. By using these equilibrium constants, the co-existence of hydromagnesite (5424) with nesquehonite in various, natural occurrences such as in weathering products of the meteorites from the Antarctic and serpentine-rich mine tailings, can be well explained. Since the stoichiometric ratio of Mg to C is higher in hydromagnesite (5424) than in nesquehonite, this finding

[1] Sandia National Laboratories is a multiprogram laboratory operated by Sandia Corporation, a Lockheed Martin Company, for the United States Department of Energy's National Nuclear Security Administration under Contract DE-AC04-94AL85000.

* Corresponding author. Fax: +1 575 234 0061.
E-mail address: yxiong@sandia.gov (Y. Xiong).

0883-2927/$ - see front matter © 2008 Elsevier Ltd. All rights reserved.
doi:10.1016/j.apgeochem.2007.12.035

could have important implications for the sequestration of anthropogenic CO_2 in mafic and ultramafic rocks, suggesting that the sequestration of anthropogenic CO_2 is optimal in the stability field of nesquehonite.
© 2008 Elsevier Ltd. All rights reserved.

1. Introduction

The reaction path for the MgO–CO_2–H_2O system at ambient temperatures and ambient atmospheric CO_2 partial pressure is of both geological interest and practical significance. From the geological point of view, knowledge of the reaction path in this system would lead to a better understanding of the low temperature alteration or weathering of mafic and ultramafic rocks. From a practical point of view, exact knowledge of the reaction path in this system is important to the performance assessment of geological repositories for nuclear wastes. Industrial-grade MgO consisting mainly of the mineral periclase is the only engineered barrier certified by the Environmental Protection Agency (EPA) for emplacement in the Waste Isolation Pilot Plant (WIPP) in the USA (US DOE, 1996), and a $Mg(OH)_2$-based engineered barrier consisting mainly of the mineral brucite is to be employed in the Asse repository in Germany (Schuessler et al., 2002). In addition, as the stoichiometry of Mg to C is different in metastable Mg carbonates, a better knowledge of the reaction path could have important implications to sequestration of anthropogenic CO_2 in mafic and ultramafic rocks.

The WIPP is located in a bedded salt formation, and the Asse repository is located in a domal salt formation. The WIPP is a US Department of Energy geological repository for the permanent disposal of defense-related transuranic (TRU) waste (US DOE, 1996). This geological repository is located 42 km east of Carlsbad in southeastern New Mexico. The repository is 655 m below the surface, and is situated in the Salado Formation, a Permian salt bed composed mainly of halite, and of lesser amounts of anhydrite, gypsum, polyhalite, magnesite, clays and quartz (Stein, 1985; US DOE, 1996). The Salado Formation is approximately 600 m thick (Powers et al., 1976). The Rustler Formation is immediately above the Salado Formation; it is 95 m thick at the WIPP and consists of anhydrite, halite, siltstone, sandstone and dolomite. The Castile Formation underlies the Salado, and is approximately 385 m thick at the WIPP (Powers et al., 1976). It has three thick anhydrite units separated by halite layers (Powers et al., 1976). There are brine reservoirs located in areas of structural deformation within the Castile Formation (Popielak et al., 1983). According to Swift and Corbet (2000), "A brine reservoir below the waste would have no effect on the disposal system as long as it remained undisturbed, but future drilling activity could result in an inadvertent borehole penetration of both repository and an underlying reservoir. Performance assessment modeling, therefore, includes the possible existence of a brine reservoir." The in situ temperature at a depth of 655 m (the repository horizon) is 28 °C (Munson et al., 1987). This is also the temperature expected after the repository is filled and sealed because the TRU waste to be emplaced in the WIPP will not produce enough heat to increase the temperature significantly. The function of the MgO engineered barrier is to consume CO_2 gas that might be generated by the microbial degradation of organic materials (cellulosic, plastic and rubber materials) in the waste and waste packages. Since the possibility of microbial generation of significant quantities of CO_2 cannot be ruled out, MgO is being emplaced to consume CO_2 and buffer the f_{CO_2} and pH of brines at values that will minimize the solubilities of actinides (mainly Th, U, Pu, and Am). It is noted here that f_{CO_2} will be employed in thermodynamic calculations, and P_{CO_2} will be used in description of experimental conditions hereafter.

The carbonation reaction path of brucite is particularly complex as Mg has a strong tendency to form a series of metastable hydrous carbonates at ambient temperatures (e.g., Lippmann, 1973; Königsberger et al., 1999). These metastable hydrous carbonates include hydromagnesite ($Mg_5(CO_3)_4(OH)_2 \cdot 4H_2O$, referred to as hydromagnesite (5424) hereafter; or $Mg_4(CO_3)_3(OH)_2 \cdot 3H_2O$, referred to as hydromagnesite (4323)); artinite ($Mg_2CO_3(OH)_2 \cdot 3H_2O$); nesquehonite ($MgCO_3 \cdot 3H_2O$); lansfordite ($MgCO_3 \cdot 5H_2O$); dypingite ($Mg_5 \cdot (CO_3)_4(OH)_2 \cdot 5(\text{or } 6)H_2O$); and barringtonite ($MgCO_3 \cdot 2H_2O$). These metastable phases are expected to convert to magnesite ($MgCO_3$) in the 10 ka period during which the repository is regulated by the EPA (magnesite is the thermodynami-

cally stable carbonate under these conditions, and is also a minor mineral in the Salado Formation). Since the free energies of formation ($\Delta_f G$) for these stable and metastable hydrous and anhydrous carbonates are different, the f_{CO_2} buffered by the assemblage of brucite and any one of these carbonates will differ. Such differences could have important implications for the performance assessment of the WIPP and other geological repositories, because f_{CO_2} could have a significant effect on actinide solubilities due to the fact that actinides can form strong complexes with carbonate ions (e.g., Grenthe et al., 1992; Silva et al., 1995; Lemire et al., 2001).

The carbonation of brucite is also important geologically because altered mafic and ultramafic rocks may contain brucite, rather than periclase owing to fast hydration rates at elevated temperatures (Kennedy, 1956). For instance, serpentites can contain brucite (e.g., Hostetler et al., 1966; Wicks and Whittaker, 1977; Neal and Stanger, 1984), and ophiolites can contain brucite as the alteration mineral (Huot et al., 2002). In addition, a better understanding of the formation of hydromagnesite may shed additional light on the "dolomite ($CaMg(CO_3)_2$) problem" because hydromagnesite, along with aragonite, seems to play the role of precursor to dolomite and magnesite ($MgCO_3$) (Lippmann, 1973).

The hydration of periclase is less complicated than the carbonation of brucite. However, knowledge of the interactions between periclase and high-ionic-strength solutions is not certain. As the ionic-strength of brines in the WIPP can be as high as ~7 M (~8 m) (Brush, 1990), a better knowledge of such interactions would benefit not only the performance assessment of geological repositories but also the understanding of alteration or weathering of mafic and ultramafic rocks in environments where high-ionic-strength solutions predominate. For example, there are fresh mafic and ultramafic rocks on Zabargad Island in the Red Sea interacting with high-ionic-strength solutions (Bonatti et al., 1986; Sciuto and Ottonello, 1995). In addition, periclase has been observed in metacarbonates such as those in the Bushveld Complex, South Africa (Buick et al., 2000) and in magnesian skarns (Zhao et al., 1999).

Both the WIPP and Asse repositories are in salt formations, and consequently, the associated brines are high-ionic-strength solutions. Therefore, exact knowledge of the reaction path in this system is important to performance assessment. This paper presents experimental results focusing on the reaction paths of brucite (and some experiments starting directly with periclase) upon its contact with solutions of various ionic strengths at room temperature and laboratory atmospheric CO_2 partial pressure ($P_{CO_2} = 4 \times 10^{-4}$ atm), which may be close to the initial partial pressure of CO_2 in the repositories when the room closure occurs. The kinetic aspect of such processes, i.e., the carbonation rates of brucite under various conditions, will be addressed elsewhere. In addition, some experiments were conducted at higher partial pressures of CO_2 ($P_{CO_2} = 5 \times 10^{-2}$ atm) to accelerate these carbonation reactions. These runs also provide better understanding of the reaction path for some environments where the partial pressure of CO_2 can be higher than that of atmospheric CO_2 partial pressure at the surface of the Earth (e.g., Hinsinger et al., 2006). It has also been inferred that siderite in the martian meteorite ALH840001 formed by interaction with Cl-rich brines at or near the surface of Mars that had P_{CO_2} ranging from 5×10^{-2} to 25×10^{-2} atm, as did siderite and smectites in some of the nakhlites (Bridges et al., 2001). Therefore, the experiments at $P_{CO_2} = 5 \times 10^{-2}$ atm would also have a bearing on secondary minerals resulting from weathering on Mars.

2. Experimental methods

The reaction path experiments were conducted at the ambient laboratory temperature (22.5 ± 1.5 °C), and ambient laboratory atmospheric concentrations of CO_2 ($P_{CO_2} = 10^{-3.4}$ atm) and $P_{CO_2} = 5 \times 10^{-2}$ atm in various solutions including deionized (DI) water; 0.010, 0.10, 1.0 and 4.4 m NaCl solutions; and ERDA-6 and Generic Weep Brine (GWB). ERDA-6 is a synthetic, NaCl-rich brine representative of brines from the Castile Formation (Popielak et al., 1983) (Table 1). GWB is a synthetic $MgCl_2$-rich brine typical of intergranular brines from the Salado Formation at or near the stratigraphic horizon of the repository (US DOE, 2004) (Table 1). The solid starting materials were primarily periclase (USP/FCC grade, purity > 96.0%) and brucite (USP/FCC grade, purity > 95.0%) from Fisher Scientific, Inc., referred to as *FMgO* and $FMg(OH)_2$, respectively, hereafter. In some experiments, as-received MgO from Premier Chemicals, Inc. in Gabbs, Nevada, was used for comparison; this starting material will be referred to as *PMgO*. Premier Chemicals supplied this MgO to the WIPP while these experiments were being conducted. *PMgO*

Table 1
Compositions of GWB and ERDA-6

Element	GWB[a]	ERDA-6[b]
B	155 mM (0.180 m)	63 mM (0.0692 m)
Na	3.48 M (4.04 m)	4.87 M (5.35 m)
Mg	1.00 M (1.16 m)	19 mM (0.0209 m)
K	458 mM (0.532 m)	97 mM (0.106 m)
Ca	14 mM (0.0163 m)	12 mM (0.0132 m)
SO_4	175 mM (0.203 m)	170 mM (0.187 m)
Cl	5.51 M (6.40 m)	4.8 M (5.27 m)
Br	26 mM (0.0302 m)	11 mM (0.0121 m)
Total inorganic C	–	16 mM (0.0176 m)
Density	1.2	1.216
TDS	–	330,000 mg/L
Ionic-strength	7.12 M (8.26 m)	5.30 M (5.82 m)

[a] From US DOE (2004); concentrations on molal scale are calculated from the density.
[b] From Popielak et al. (1983); concentrations on molal scale are calculated from the density.

contains a minimum of 90 wt% periclase and a minimum of 95 wt% of periclase and lime, with the rest as accessory phases (US DOE, 2004, Appendix BARRIERS). These accessory phases may include oxides and silicates such as spinel ($MgAl_2O_4$), ulvöspinel ($Ti(Fe,Mg)_2O_4$), forsterite (Mg_2SiO_4), and monticellite ($CaMgSiO_4$). These results are based on characterization of Premier MgO by Bryan and Snider (2001). It is expected that periclase and lime will react rapidly with any CO_2 produced by possible microbial consumption of cellulosic, plastic, and rubber materials; and that the accessory oxides and silicates could also react with CO_2 to a significant extent during the 10 ka regulatory period.

In static experiments at ambient temperature and P_{CO_2}, the mass of solid starting materials varied from 2 to 5 g. "Static experiments" means that neither solutions nor solid starting materials were agitated by any means. The solid-to-solution mass ratio ranged from 4×10^{-2} to 9×10^{-2}. The caps of the containers were closed loosely in order to allow atmospheric CO_2 to enter and react with the solutions. The masses of the solutions were closely monitored to compensate for the loss of water through evaporation. After the termination of each run, the solid reaction products were filtered by vacuum filtration and rinsed with DI water, and the solutions were saved for chemical analysis. The solid reaction products were dried at room temperature and then ground with a mortar and pestle for identification of mineral phases.

Some experiments were conducted with agitation accomplished by continuously bubbling compressed air into the solutions, some with and some without continuous mixing by a stir bar. The comparison of the results from static and agitated experiments could provide information regarding the relative kinetics of the reaction paths under these conditions.

For runs at the laboratory room temperature and $P_{CO_2} = 5 \times 10^{-2}$ atm, the starting materials and solutions were contained in 125-mL polypropylene bottles. Each bottle contained 5 g of one of the following solids: *PMgO*, *FMgO*, prehydrated and crushed Premier Chemicals MgO (*PB*) (i.e., periclase converted to brucite), and prehydrated and crushed Fisher MgO (*FB*). Prehydrated samples were prepared by adding 5 g of either crushed *PMgO* or *FMgO* to 100 mL of brine (either ERDA-6 or GWB, depending on the brine used for subsequent carbonation experiments). The bottles were tightly closed and placed in a 90 °C oven for approximately 3–4 weeks. Before the prehydrated samples were added to plastic containers connected to a manifold, a small portion of the sample was analyzed for brucite.

All experiments at the laboratory room temperature and $P_{CO_2} = 5 \times 10^{-2}$ atm were placed in a glove box with a controlled atmosphere. The partial pressure of CO_2 in the glove box was controlled by pumping premixed 5% CO_2 and 95% N_2 into the glove box at 500 mL/min. To bring the glove box up to 5% CO_2 in a timely fashion after it was opened for sampling, dilute H_2SO_4 (0.30 m) was mixed with solid $NaHCO_3$ within the glove box, which released a predetermined amount of CO_2 to the atmosphere. The 5% CO_2 was continuously bubbled into the solutions. The atmosphere in the glove box was monitored frequently with a Bacharach CO_2 analyzer.

In another independent set of experiments, experimental runs were set up in test tubes under the conditions identical to those of the static runs in order to monitor the saturation states of various Mg phases in solutions. They were placed onto an INNOVA 2100 Platform Shaker (New Brunswick Scientific, Inc.) at a shaking speed of 140 rpm. These runs were sampled periodically (usually weekly) for determination of Mg content (and impurities such as Ca content in cases where *PMgO* was used) and pH. In NaCl solutions with ionic-strength higher than 0.10 m, H^+-ion concentrations (pcH) instead of pH were determined from pH readings from the pH glass electrode. The pH was measured with an Orion-Ross combination pH glass elec-

trode. After a pH measurement was taken, approximately 3 mL of solution was withdrawn from an experimental run. The solution was filtered using a 0.2 μm syringe filter. The filtered solution was then weighed and acidified with 0.5 mL of concentrated HNO_3 (TraceMetal grade from Fisher Scientific). The solution was then diluted to 10 mL with DI water for chemical analyses.

The identification of solid phases in the reaction products was made by using a Bruker AXS, Inc., D8 Advance X-ray diffractometer (XRD) with a Kevex detector. All XRD patterns were collected using Cu Kα radiation at a scanning rate of 1.33°/min for a 2θ range of 10–90°. The reliance on the XRD technique in this study is based upon the fact that the XRD is a robust technique, and it provides definite phase identifications for crystalline phases whose concentrations are usually ⩾ a few weight percent. In addition, in order to address the possibility that minor phase(s) could be missed because of the relatively high detection limit of XRD, samples were also analyzed using a JEOL JSM-5900LV scanning electron microscope (SEM) with an energy dispersive spectroscopy (EDS) of the ThermoNORAN Vantage digital acquisition system. No minor phase was found.

The chemical analyses of solutions were performed using a Perkin–Elmer dual-view inductively coupled plasma-atomic emission spectrometer (ICP-AES) (Perkin–Elmer DV 3300). Calibration blanks and standards were precisely matched with experimental matrices. The correlation coefficients of calibration curves in all measurements were better than 0.9995. The detection limit was better than 0.06 mg/L. The analytical precision was better than ±1.00% in terms of the relative standard deviation (RSD) based on replicate analyses.

2.1. Hydrogen ion concentration measurements

In NaCl solutions with ionic-strength higher than 0.10 m, H^+-ion concentrations were measured from pH readings from the pH glass electrode. Rai et al. (1995) have conducted extensive studies to investigate the correction factors (A) in the following equation in concentrated NaCl and Na_2SO_4 electrolytes for various Orion-Ross combination electrodes.

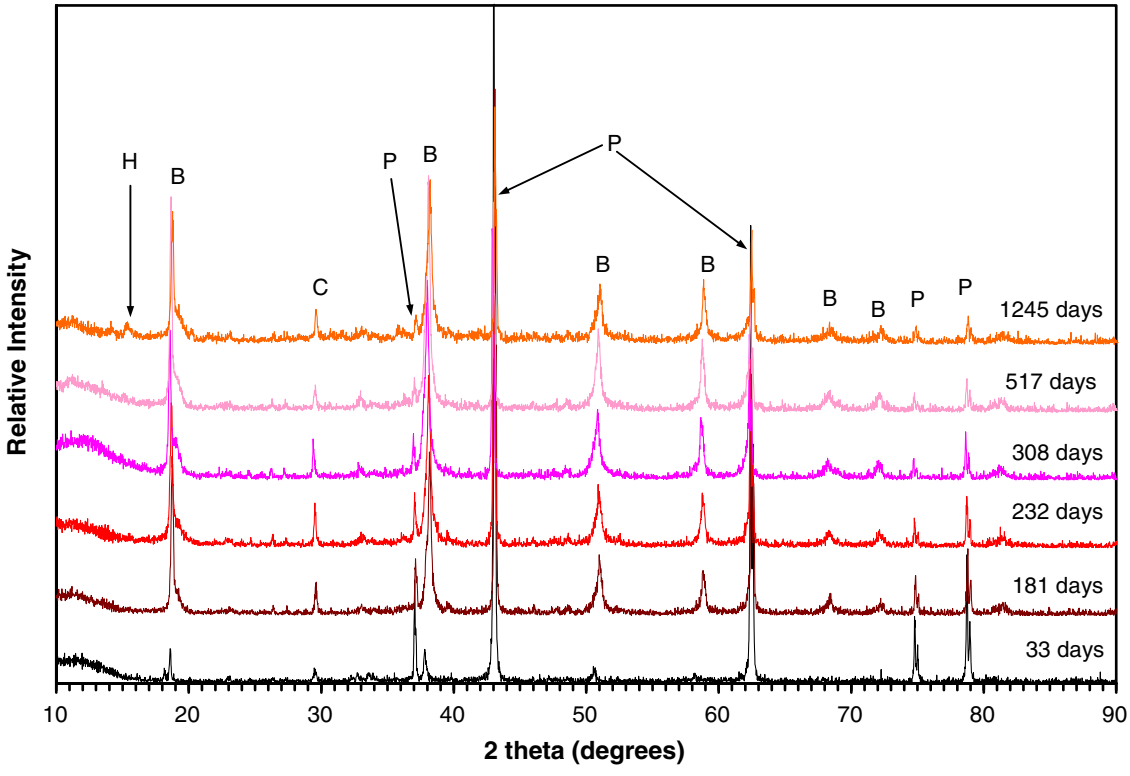

Fig. 1. XRD patterns for static experiments started with *PMgO* and DI water at laboratory ambient temperature and atmospheric CO_2 partial pressure. Abbreviations: B = brucite, C = calcite, H = hydromagnesite (5424), and P = periclase.

The relationship between the pH electrode reading (pH_{ob}) and pcH can be expressed as (Rai et al., 1995):

$$pcH = pH_{ob} + A \quad (1)$$

In Eq. (1), A is defined as:

$$A = \log \gamma_{H^+} + (F/2.303RT)\Delta E_j \quad (2)$$

where γ_{H^+} is the activity coefficient of H^+, and ΔE_j is the difference in liquid junction potential between standards and solution. Both terms on the right-hand side of Eq. (2) are not individually measurable, but the combination can be measured.

The linear relation between A and concentrations for NaCl solutions, valid up to 6.0 m obtained by Rai et al. (1995), is expressed as:

$$A = 0.159X \quad (3)$$

where X is the NaCl concentration in molality. They also performed a study to evaluate the dependence of the parameter A on an individual electrode by using a limited number of different Orion-Ross electrodes. They concluded that "the A values did not differ significantly for different electrodes", and that the linear relation between A and concentrations of NaCl and Na_2SO_4 obtained can be applied to different NaCl and Na_2SO_4 solutions "without having to calibrate each and every electrode."

Therefore, the experimentally measured pH readings in this study (pH_{ob}) in experiments using pure NaCl matrixes are corrected with the values of A at the corresponding concentrations of NaCl solutions by using Eq. (3).

3. Results and discussion

3.1. Reaction path starting with periclase at atmospheric CO_2 partial pressure

Reaction paths in static runs at atmospheric CO_2 partial pressure in various solutions containing Premier MgO are elucidated in the following series of figures. Fig. 1 displays experimental results from runs using DI water. It is clear from Fig. 1 that some brucite formed by 33 days. Fig. 2 shows experimental results in 4.4 m NaCl solution. Brucite formed by 76 days. Fig. 3 suggests that

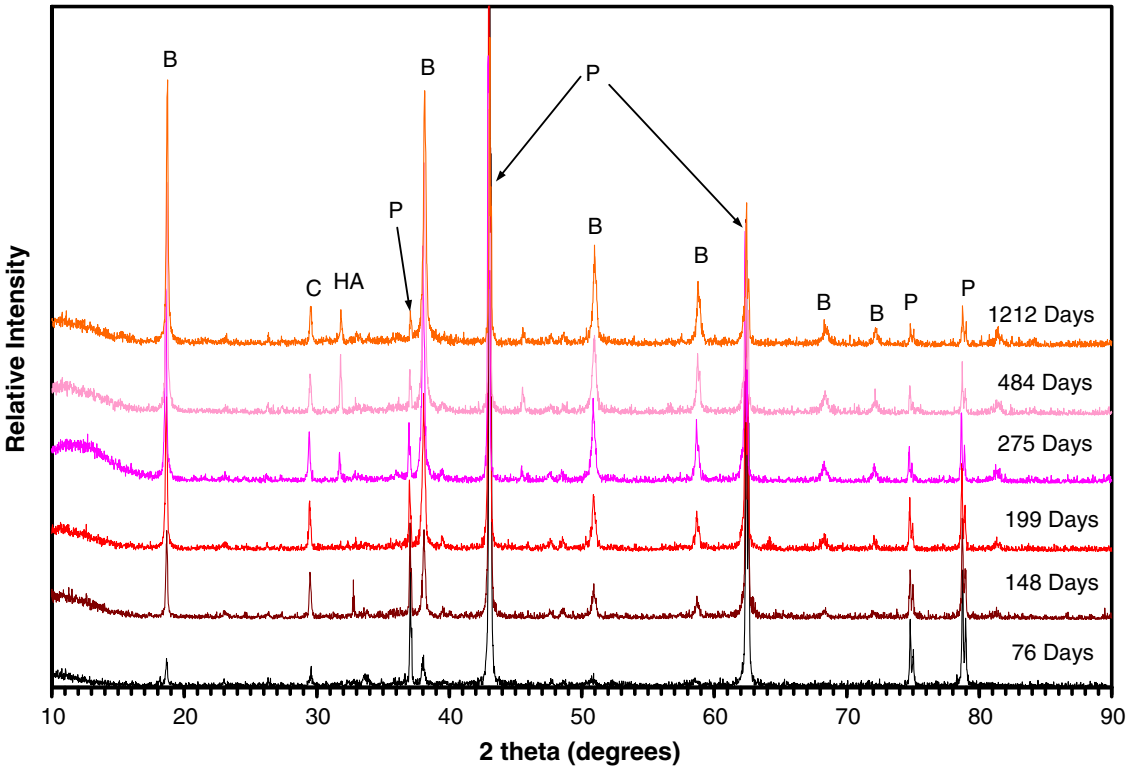

Fig. 2. XRD patterns for static experiments started with *PMgO* and 4.4 m NaCl solution at laboratory ambient temperature and atmospheric CO_2 partial pressure. Abbreviation: HA = halite; other abbreviations are the same as those in Fig. 1.

brucite formed between 16 and 50 days in ERDA-6. Fig. 4 demonstrates that brucite formed between 50 and 126 days in GWB. Comparison of these figures suggests that brucite crystallized more rapidly in low-ionic-strength solutions in the experiment started with DI water than in experiments with high-ionic-strength solutions. The faster conversion in low-ionic-strength solutions can be attributed to the higher activity of water in low-ionic-strength solutions according to the following reaction:

$$\mathrm{MgO(periclase) + H_2O(l) = Mg(OH)_2(brucite)} \tag{4}$$

The reaction path in the hydration of periclase in GWB is slightly different than in DI water, NaCl, and ERDA-6. Fig. 4 shows that Mg chloride hydroxide hydrate ($Mg_3(OH)_5Cl \cdot 4H_2O$) also formed in addition to brucite. $Mg_3(OH)_5Cl \cdot 4\,H_2O$ and $Mg_2Cl(OH)_3 \cdot 4H_2O$ are major reaction products for hardening and strengthening in Mg oxychloride cements (e.g., Zhang et al., 1991; Deng and Zhang, 1999). To authors' knowledge, thermodynamic data for $Mg_3(OH)_5Cl \cdot 4H_2O$ are not well defined. However, the formation of this phase can be rationalized by using $Mg_2Cl(OH)_3 \cdot 4H_2O$ in Harvie et al. (1984) as an analogue.

The dissolution of $Mg_2Cl(OH)_3 \cdot 4H_2O$ can be expressed as:

$$\begin{aligned} &\mathrm{Mg_2Cl(OH)_3 \cdot 4H_2O + 3H^+ = 2Mg^{2+}} \\ &\quad + 7\mathrm{H_2O(l) + Cl^-} \\ &\log K_5 = 2\log a_{\mathrm{Mg^{2+}}} + 7\log a_{\mathrm{H_2O}} \\ &\quad + \log a_{\mathrm{Cl^-}} + 3\mathrm{pH} = 26.03 \end{aligned} \tag{5}$$

where $a_{Mg^{2+}}$, a_{H_2O} and a_{Cl^-} refer to activities of Mg^{2+}, H_2O and Cl^-, respectively, and the equilibrium constant for Reaction (5) ($\log K_5$) is from the HMW (Harvie-Møller-Weare) database (Harvie et al., 1984) in the EQ3/6 software package (Wolery, 1992a). Using EQ3NR (Wolery, 1992b) and the speciation and the solubility code in the Fracture-Matrix Transport software package (Novak, 1996), the predicted a_{H_2O}, $a_{Mg^{2+}}$, a_{Cl^-} and pH for GWB prior to the reaction with periclase are 0.73, 1.64, 9.88, and 7.81, respectively. For these values of a_{H_2O}, $a_{Mg^{2+}}$, a_{Cl^-}, and $\log K_5$, a pH of 8.52 is required for precipitation of $Mg_2Cl(OH)_3 \cdot 4H_2O$ in GWB.

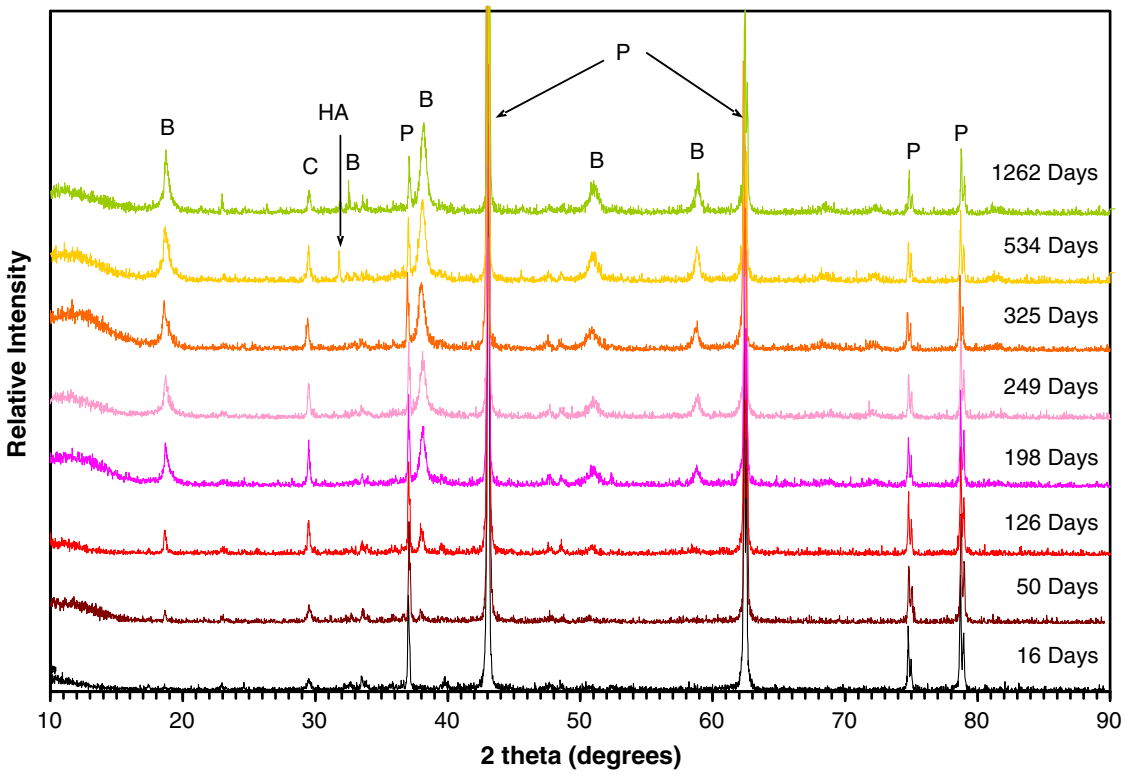

Fig. 3. XRD patterns for static experiments started with *PMgO* and ERDA-6 at laboratory ambient temperature and atmospheric CO_2 partial pressure. Abbreviations are the same as those in Figs. 1 and 2.

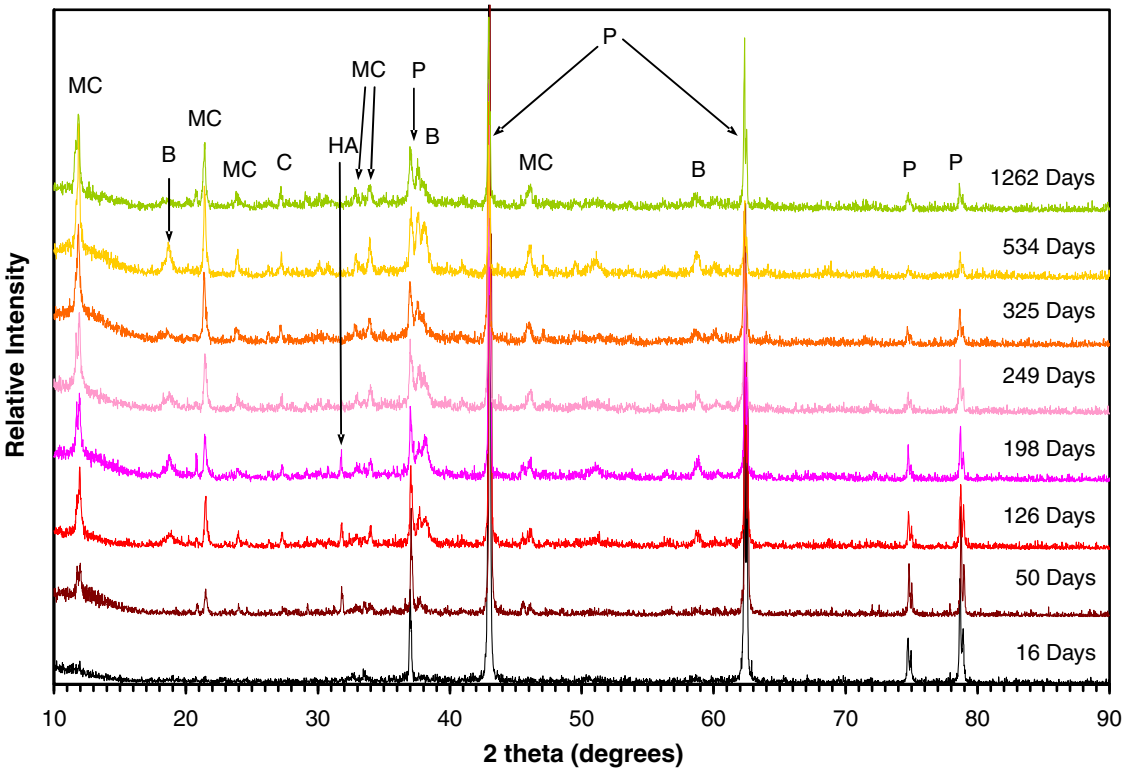

Fig. 4. XRD patterns for static experiments started with *PMgO* and GWB at laboratory ambient temperature and atmospheric CO_2 partial pressure. Abbreviation: MC = Mg chloride hydroxide hydrate; other abbreviations are the same as those in Figs. 1 and 2.

Therefore, $Mg_2Cl(OH)_3 \cdot 4H_2O$ or a similar phase, $Mg_3(OH)_5Cl \cdot 4H_2O$, would not be precipitated from GWB without the introduction of periclase and hydration of periclase to form brucite. Only after the addition of periclase/brucite can $Mg_2Cl(OH)_3 \cdot 4H_2O$ or $Mg_3(OH)_5Cl \cdot 4H_2O$ be precipitated from GWB. The fact that $Mg_3(OH)_5Cl \cdot 4H_2O$ is formed in GWB implies that the formation of $Mg_3(OH)_5Cl \cdot 4H_2O$ is favored over $Mg_2Cl(OH)_3 \cdot 4H_2O$ in complex brines such as GWB. However, determination of the relative stabilities of $Mg_3(OH)_5Cl \cdot 4H_2O$ and $Mg_2Cl(OH)_3 \cdot 4H_2O$, as expressed by the reaction,

$$Mg_3(OH)_5Cl \cdot 4H_2O + 2H^+ = Mg^{2+} + Mg_2Cl(OH)_3 \cdot 4H_2O + 2H_2O \quad (6)$$

requires future study.

Furthermore, the reason why $Mg_3(OH)_5Cl \cdot 4H_2O$ was not formed in experiments in ERDA-6 is similar to that described above. The values of a_{H_2O}, $a_{Mg^{2+}}$, a_{Cl^-} and pH predicted for ERDA-6 prior to reaction with periclase are 0.75, 3.31×10^{-2}, 5.08, and 6.17, respectively. For these values, a pH of 9.68 is required for precipitation of $Mg_2Cl(OH)_3 \cdot 4H_2O$ in ERDA-6. Such a pH value would not be attained by hydration of periclase to form brucite in ERDA-6. This may be the reason why $Mg_3(OH)_5Cl \cdot 4H_2O$ was not observed in the experiments in ERDA-6.

Fig. 5 illustrates the results in the agitated runs. It is clear from Fig. 5 that hydromagnesite (5424) appeared at 327 days. In the run started with DI water, XRD patterns of hydromagnesite (5424) can be seen. In comparison, only small peaks of hydromagnesite (5424) appeared in the static run terminated at 1245 days (Fig. 1). Enhanced mass transport facilitated by continuous bubbling of compressed air apparently resulted in more rapid carbonation. It should be noted that XRD peaks of brucite do not appear in Fig. 5 because only the upper portion of the slurries was sampled; these did not contain brucite because the density of brucite (2.38 g cm^{-3}) is greater than that of hydromagnesite (5424) (2.16 g cm^{-3}).

3.2. Reaction path starting with brucite at atmospheric CO_2 partial pressure

Figs. 6–12 show the reaction paths for carbonation of brucite in different solutions with varying

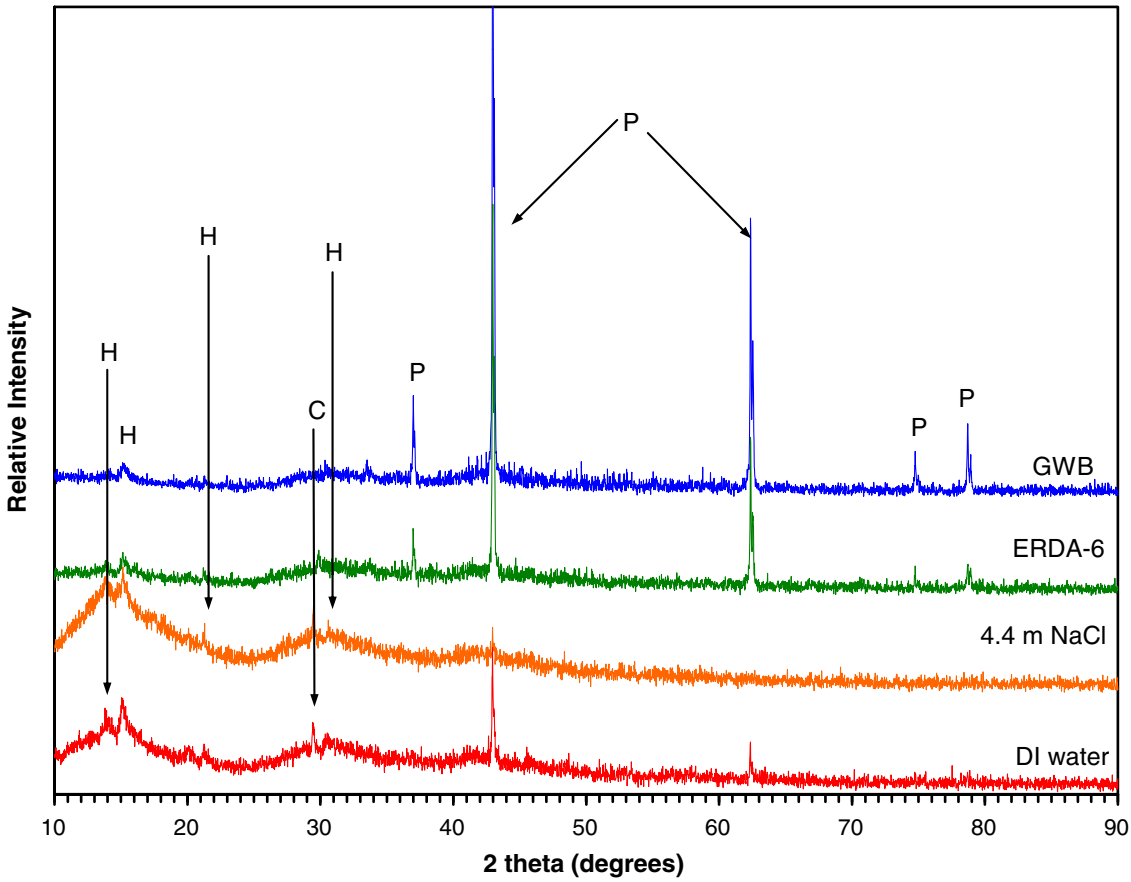

Fig. 5. XRD patterns for stirred experiments at laboratory ambient temperature started with *PMgO* and DI water, 4.4 m NaCl, ERDA-6, and GWB at a run time of 327 days. Compressed air was continuously bubbled into solutions. Abbreviations are the same as those in Fig. 1.

ionic strengths. Fig. 6A shows that the conversion from brucite to hydromagnesite (5424) was rapid under agitated conditions obtained by bubbling compressed air into solutions and continuously stirring the slurry. Well-developed XRD patterns of hydromagnesite (5424) were observed at 46 days. At about 181 days, brucite was almost totally converted to hydromagnesite (5424), as indicated by the disappearance of major peaks of brucite. In contrast, the conversion from brucite to hydromagnesite (5424) was slower in the static experiment started with DI water (Fig. 6B). XRD peaks for hydromagnesite (5424) were observed only by 189 days.

The results presented in Figs. 7–12 are from static experiments. Fig. 7 indicates that the pattern of hydromagnesite (5424) was not obvious in the 0.010 m NaCl solution at 126 days. At 217 days, XRD peaks of hydromagnesite (5424) appeared. Similarly, Fig. 8 shows that in the 0.10 m NaCl solution, peaks of hydromagnesite (5424) are discernable in the pattern obtained from the sample with a run time of 217 days. In the 1.0 m NaCl solution, Fig. 9 shows that the formation of hydromagnesite (5424) was not detected by XRD until the run time reaching 314 days. A well-developed XRD pattern of hydromagnesite (5424) was observed at 340 days. In the 4.4 m NaCl solution, the formation of hydromagnesite (5424) was slower than that in other solutions with lower ionic-strength (Fig. 10). The formation of hydromagnesite (5424) was detectable by XRD at a run time of 423 days. The rate of the formation of hydromagnesite (5424) in ERDA-6 (Fig. 11) was similar to that in 4.4 m NaCl, and the detection of its presence by XRD required at least 368 days. Similarly in GWB (Fig. 12), the formation of hydromagnesite (5424) was slow.

It is of interest to note that in addition to hydromagnesite (5424), Mg chloride hydroxide hydrate ($Mg_3(OH)_5Cl \cdot 4\,H_2O$) was also formed in GWB at 368 days (Fig. 12), as suggested by Eq. (5). Again,

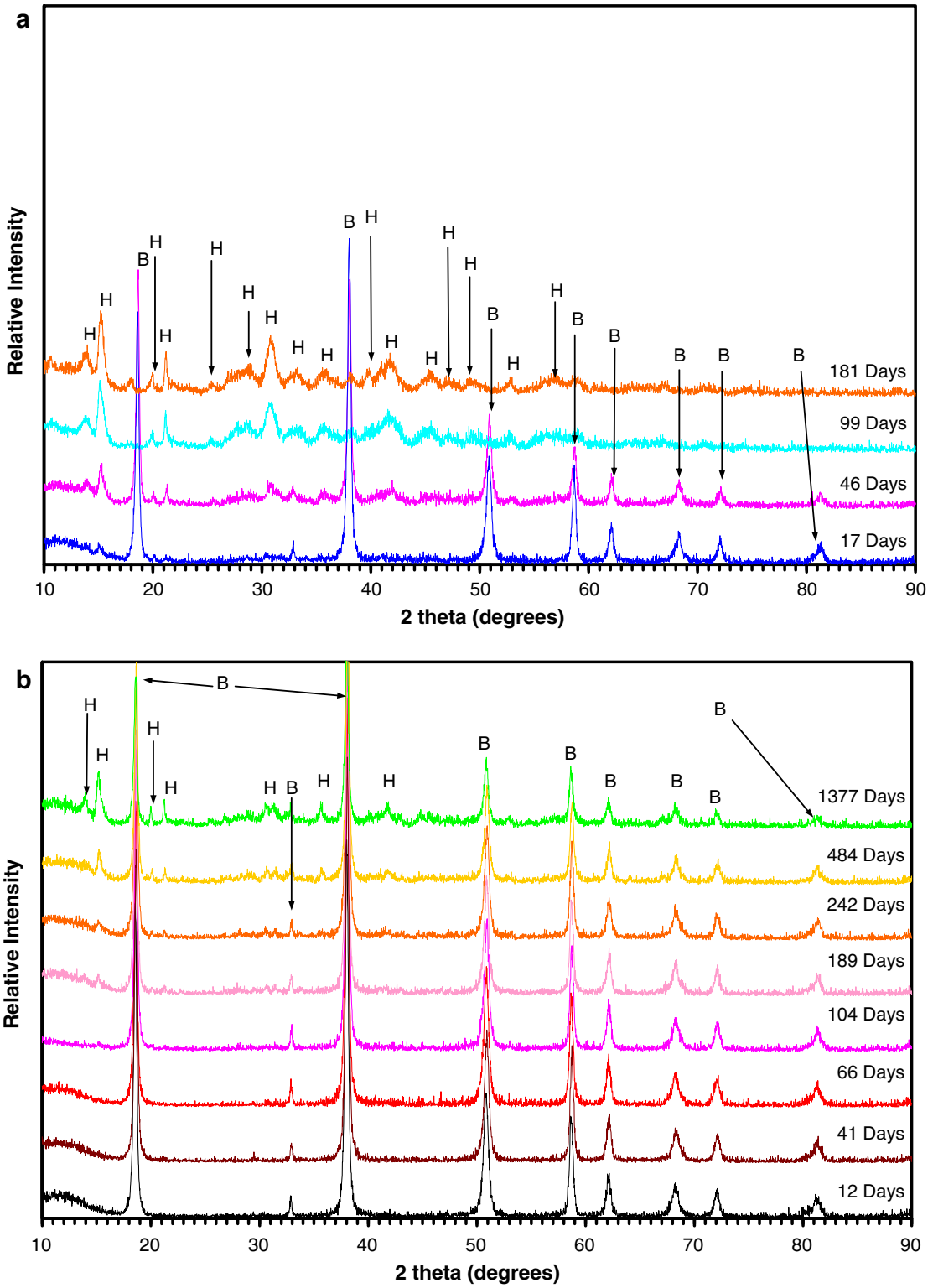

Fig. 6. XRD patterns for experiments at laboratory ambient temperature started with $FMg(OH)_2$ and DI water. (A) Stirred experiments in which compressed air was continuously bubbled into solutions with slurries continuously stirred by stir bars. (B) Static runs at laboratory ambient atmospheric CO_2 partial pressure. Abbreviations are the same as those in Fig. 1.

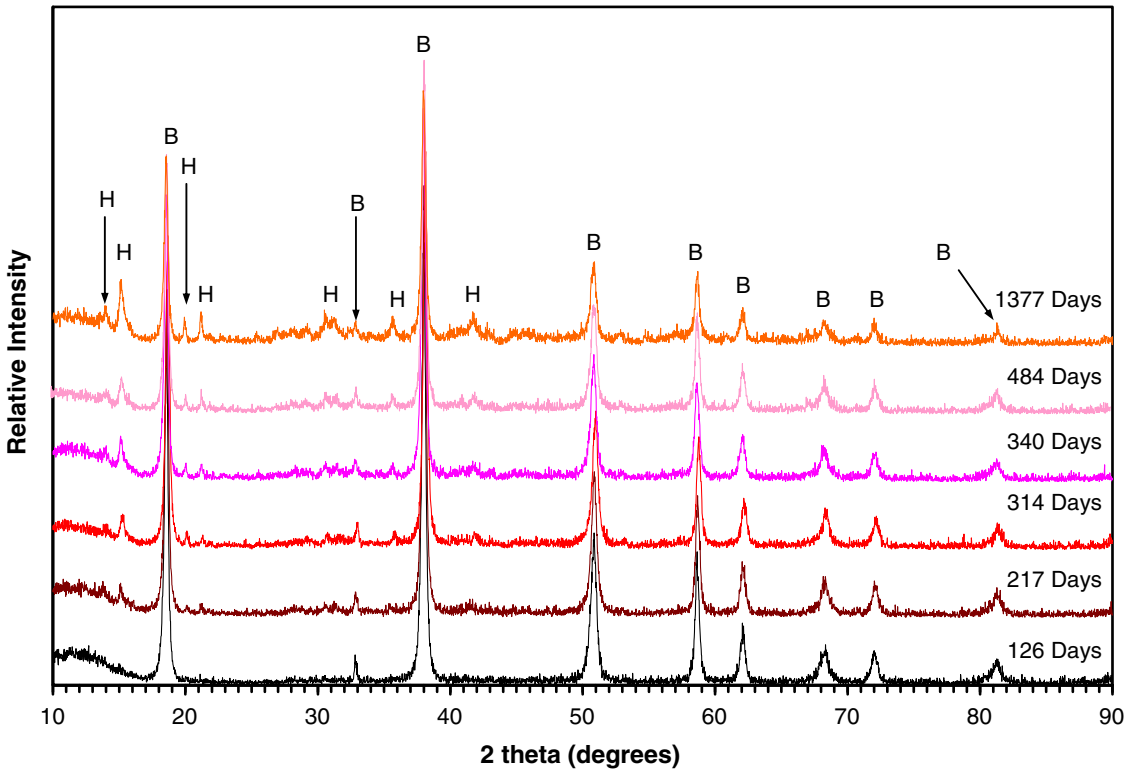

Fig. 7. XRD patterns for static experiments started with $FMg(OH)_2$ and 0.010 m NaCl solution at laboratory ambient temperature and atmospheric CO_2 partial pressure. Abbreviations are the same as those in Fig. 1.

this implies that the addition of brucite to GWB raised the pH of the brine, resulting in supersaturation of $Mg_3(OH)_5Cl \cdot 4H_2O$.

3.3. Reaction path starting with periclase at P_{CO_2} of $5 \times 10^{-2.0}$ atmospheres

The results presented in Figs. 13–16 are from stirred experiments. Figs. 13 and 14 show XRD patterns in experiments starting with *FMgO* in ERDA-6 and GWB, respectively. In runs with ERDA-6, periclase apparently was converted to brucite and nesquehonite after 1 day (Fig. 13). Then, at 91 days, hydromagnesite (5424) started to form. The co-existence of nesquehonite with hydromagnesite (5424) can be clearly seen in the run up to 303 days. At 333 days, the peaks of nesquehonite became weaker, but were still present.

In experiments in GWB (Fig. 14), brucite formed first and hydromagnesite (5424) started to form at 91 days. Nesquehonite was never detected in these runs, implying that the formation of nesquehonite is not favored in Mg-dominated, high-ionic-strength solutions such as GWB. For detailed explanations, see the following section regarding the relative stability of hydromagnesite (5424) and nesquehonite.

3.4. Reaction path starting with brucite at P_{CO_2} of $5 \times 10^{-2.0}$ atmospheres

Figs. 15 and 16 show XRD patterns in experiments using prehydrated *FMgO* in ERDA-6 and GWB, respectively. In ERDA-6 (Fig. 15), nesquehonite started to form between 1 and 3 days. Hydromagnesite (5424) started to form between 7 and 21 days. The peaks of nesquehonite became weaker after 21 days. At 333 days, nesquehonite is still present, albeit the peak is weaker.

In GWB, hydromagnesite (5424) appeared to form between 7 and 21 days (Fig. 16). After 91 days, well-developed XRD patterns of hydromagnesite (5424) can be seen. Similar to the runs starting with periclase in GWB (Fig. 14), nesquehonite was never observed in these runs, implying again that Mg-dominated solutions with high-ionic-strength ($\geqslant$8 m) do not favor the formation of nesquehonite.

In the experiments in GWB at $P_{CO_2} = 5 \times 10^{-2}$ atm using either periclase or brucite as starting

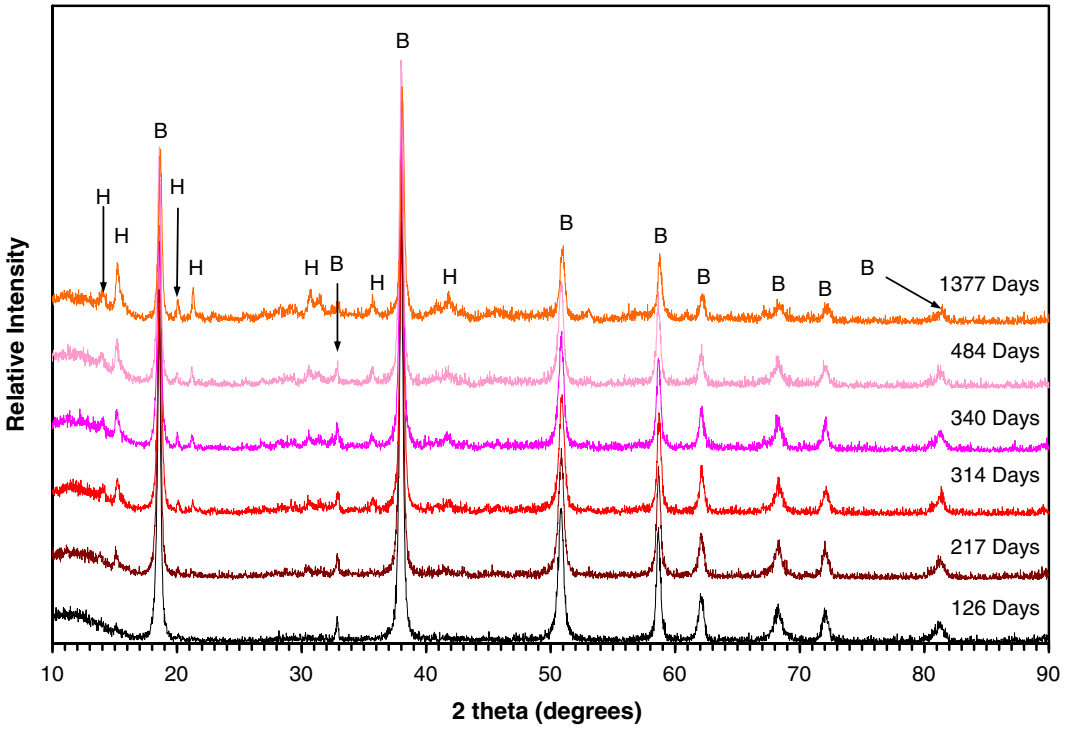

Fig. 8. XRD patterns for static experiments started with $FMg(OH)_2$ and 0.10 m NaCl solution at laboratory ambient temperature and atmospheric CO_2 partial pressure.Abbreviations are the same as those in Fig. 1.

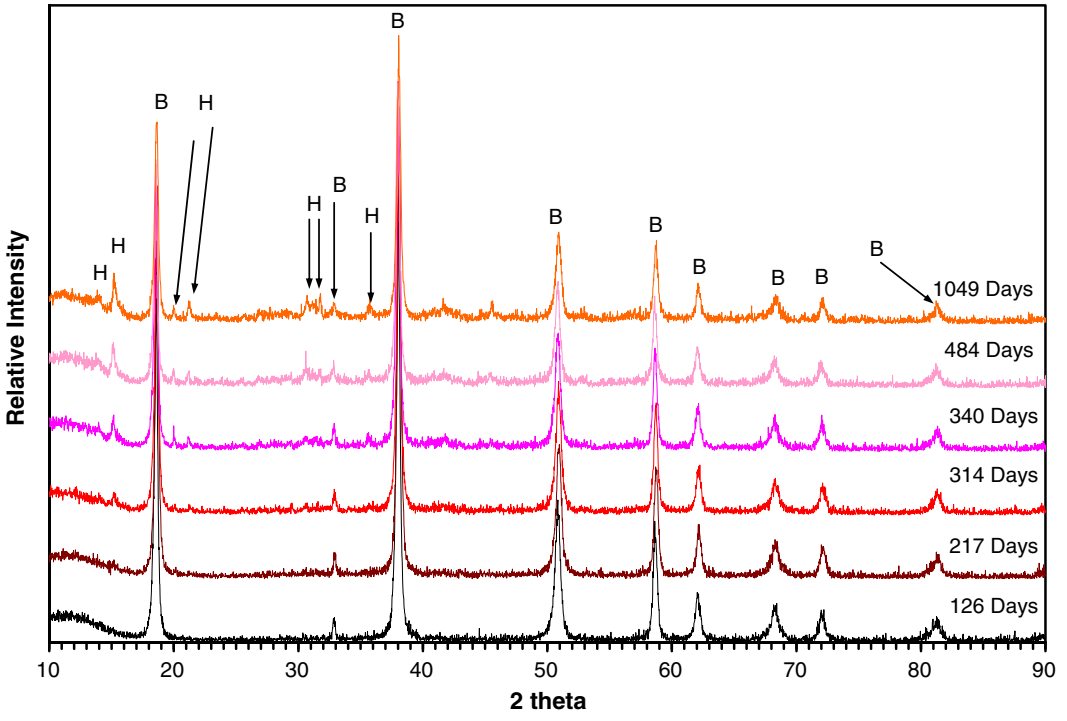

Fig. 9. XRD patterns for static experiments started with $FMg(OH)_2$ and 1.0 m NaCl solution at laboratory ambient temperature and atmospheric CO_2 partial pressure. Abbreviations are the same as those in Fig. 1.

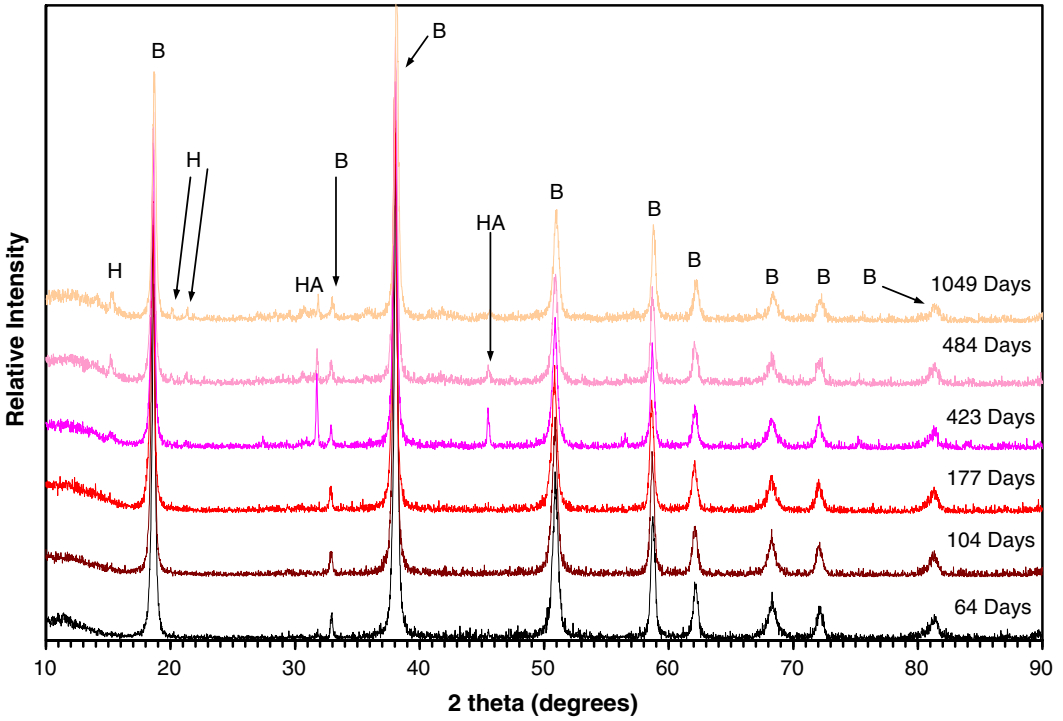

Fig. 10. XRD patterns for static experiments started with $FMg(OH)_2$ and 4.4 m NaCl solution at laboratory ambient temperature and atmospheric CO_2 partial pressure. HA = halite; other abbreviations are the same as those in Fig. 1.

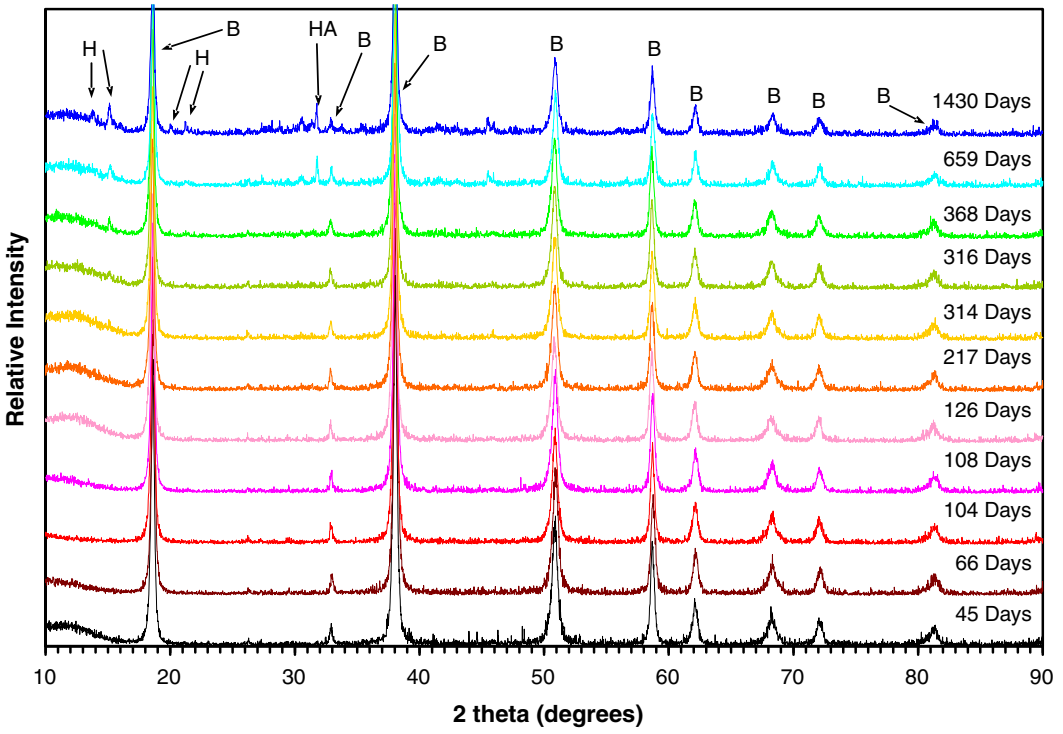

Fig. 11. XRD patterns for static experiments started with $FMg(OH)_2$ and ERDA-6 at laboratory ambient temperature and atmospheric CO_2 partial pressure. HA = halite; other abbreviations are the same as those in Fig. 1.

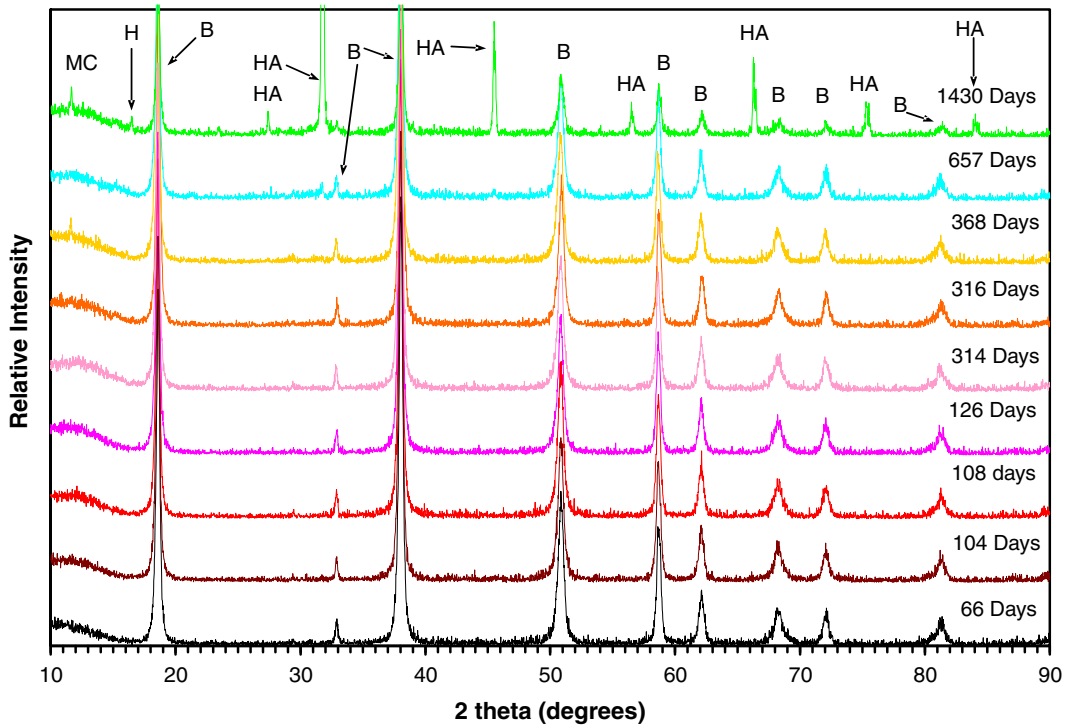

Fig. 12. XRD patterns for static experiments started with $FMg(OH)_2$ and GWB at laboratory ambient temperature and atmospheric CO_2 partial pressure. Abbreviations are the same as those in Figs. 1 and 4.

material, the formation of $Mg_3(OH)_5Cl \cdot 4H_2O$ was not observed. This situation is different from the observations in the runs at atmospheric CO_2 using the same starting material and same starting brine.

3.5. Thermodynamic modeling

3.5.1. Saturation Indices

By the using the experimental data tabulated in Appendix A (supplementary material available on web), the saturation states with respect to brucite, hydromagnesite (5424), hydromagnesite (4323) and nesquehonite are calculated for the independent set of experiments. Note that pcH values were obtained in those experiments in NaCl solutions (Appendix A) according to the method described in Section 2. Figs. 17–19 illustrate the saturation indices (SI) for 4 Mg phases, i.e., brucite, hydromagnesite (5424), hydromagnesite (4323), and nesquehonite, by performing EQ3NR calculations (Version 7.2c; Wolery, 1992b; EQ3NR modeling was done under SNL software QA requirements). The database used is modified from the HMW database by incorporating the thermodynamic data for hydromagnesite (4323) from Langmuir (1965) and hydromagnesite (5424) from Robie and Hemingway (1973). SI is defined as

$$SI = \log(Q/K_{sp}) \quad (7)$$

where Q is the ion activity product, and K_{sp} is the solubility product of a given phase. SI is an indicator of the saturation state with respect to the solid phase of interest in a solution. If $SI < 0$, the solution is undersaturated with that phase. If $SI = 0$, the solution is saturated with that phase. If $SI > 0$, it means that the solution is oversaturated. In the modeling, experimentally determined concentrations of Mg and H^+ were used as inputs (Appendix A) in addition to the background electrolytes. Dissolved CO_2 concentrations are calculated by choosing the option of the charge balance on HCO_3^- in the code.

Fig. 17A and B present SI for experiments started with $FMgO$ in DI water and 4.4 m NaCl solution. The SI for hydromagnesite (5424 and 4323) can be up to about 3 orders of magnitude higher with DI water than with 4.4 m NaCl solution, in general. However, there is a considerable overlap between the SIs for these two solutions. Both solutions were at or near equilibrium with brucite up to 250 days.

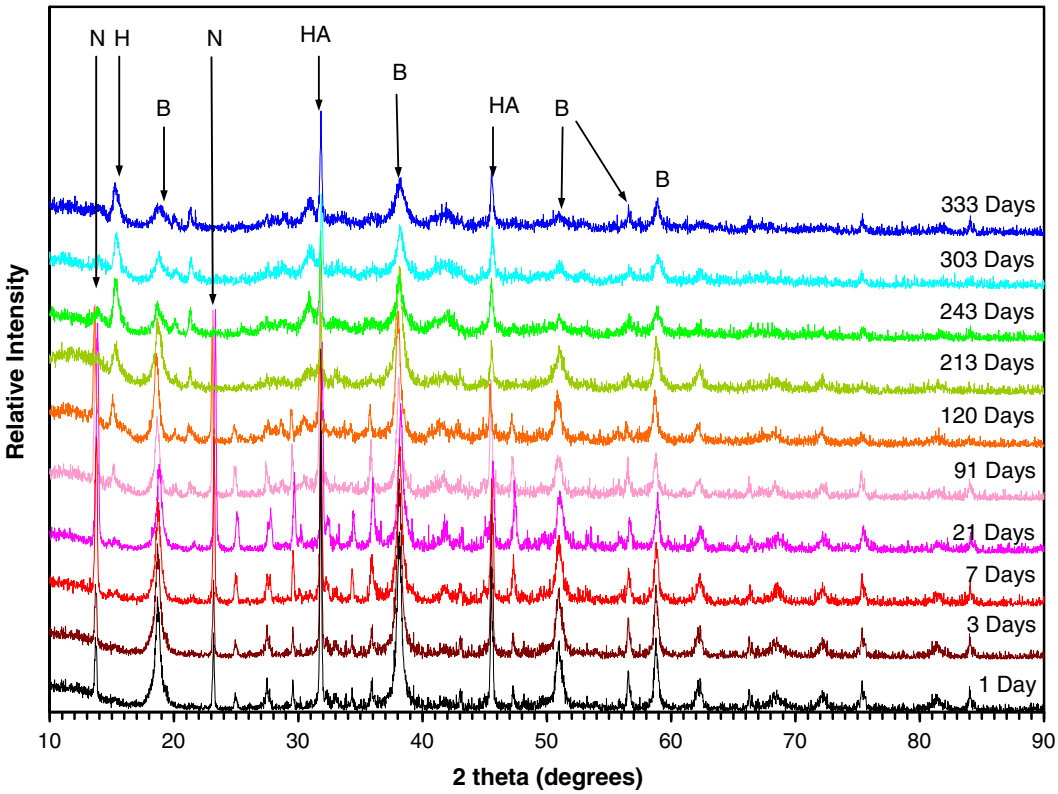

Fig. 13. XRD patterns for stirred experiments started with *FMgO* at $P_{CO_2} = 5 \times 10^{-2}$ atm in ERDA-6. A mixture of 5 vol.% CO_2 with 95 vol.% N_2 gas was bubbled into the solution. Abbreviation: N = nesquehonite, other abbreviations are the same as those in Figs. 1 and 2.

After about 333 days, both solutions were slightly undersaturated with brucite. Nesquehonite was always an undersaturated phase throughout the experiment. In addition, the SI for nesquehonite in 4.4 m NaCl is lower than those with DI water.

In Fig. 18A through 18D, SI is presented for experiments in NaCl solutions ranging from 0.010 m to 4.4 m using *PMgO*. In all experiments, the solutions were undersaturated with respect to nesquehonite.

Fig. 19A and B show SI for runs using $FMg(OH)_2$ as starting material in DI water and 4.4 m NaCl, respectively. The degree of supersaturation with respect to hydromagnesite in DI water can be up to about one order of magnitude higher than that in 4.4 m NaCl. However, there are overlaps in SI between these two solutions.

3.5.2. Ionic-strength effect on reaction progress

Ionic-strength has a profound effect on the reaction progress in the carbonation of brucite, as demonstrated by the systematic studies in solutions with ionic-strength ranging from those of DI water to 4.4 m NaCl. These studies indicate that the carbonation of brucite to form hydromagnesite (5424) is more rapid in solutions with lower ionic strengths. To have a better understanding of this effect, analytical data from the aforementioned experiments under static conditions were employed to conduct EQ3NR calculations. Some important species for the samplings at 404 and 426 days are listed in Table 2. It is worthwhile noting that CO_2(aq) and a_{H_2O} have a negative correlation with ionic-strength (Table 2). This may imply that CO_2(aq) and a_{H_2O} are the key factors in controlling the kinetics of the carbonation of brucite, as the above experimental results have qualitatively demonstrated that the lower the ionic-strength in the aqueous medium, the more rapid the conversion from brucite to hydromagnesite (5424).

3.5.3. Applications to nuclear waste repository

In the WIPP disposal system, the major function of the engineered barrier is to sequester CO_2

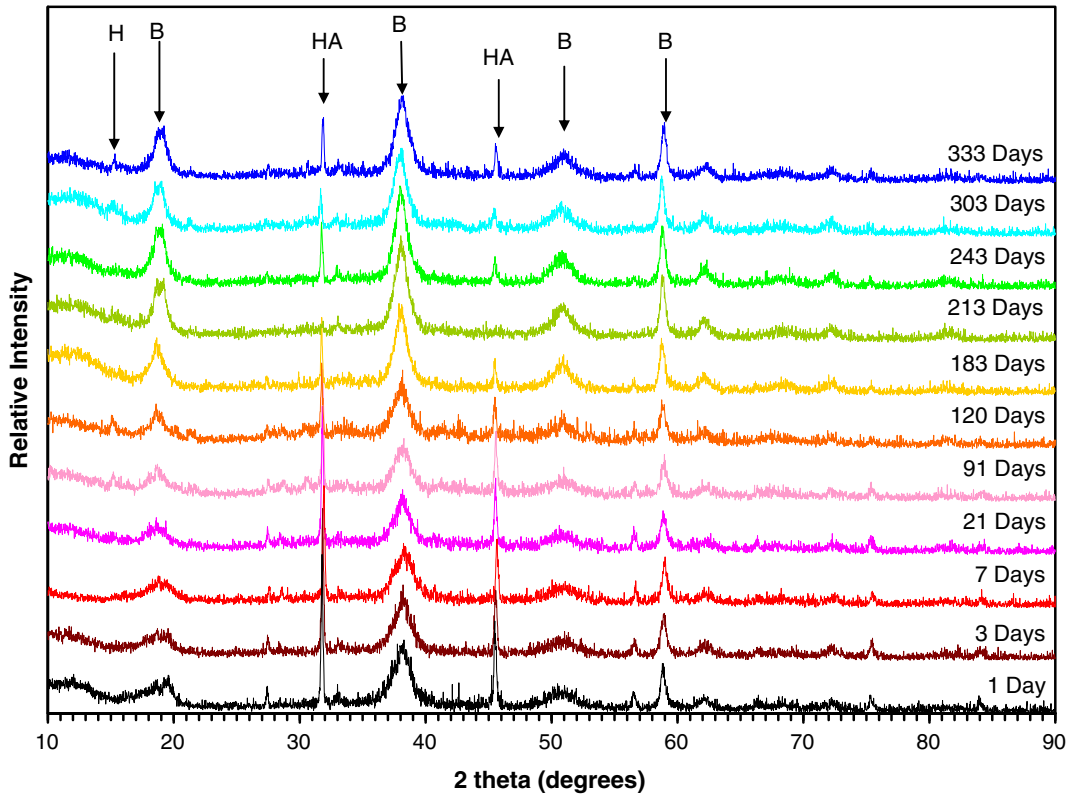

Fig. 14. XRD patterns for stirred experiments started with *FMgO* at $P_{CO_2} = 5 \times 10^{-2}$ atm in GWB. A mixture of 5 vol.% CO_2 with 95 vol.% N_2 gas was bubbled into the solution. Abbreviations are the same as those in Figs. 1 and 2.

generated by possible microbial degradation of organic materials in the waste and the waste packages via carbonation of brucite to form Mg carbonate phase(s) and to buffer the pH of the repository. In Table 3, predicted values of f_{CO_2} buffered by the assemblage of brucite and various Mg carbonates are listed. In the design, the engineered barrier is in excess relative to CO_2 to be sequestered. As the rates of carbonation of brucite are orders of magnitude higher than the rates of the possible microbial generation of CO_2 (Xiong and Snider, 2003), metastable hydromagnesite (5424) is the most likely phase to be formed in the repository. Therefore, the f_{CO_2} will be buffered by the assemblage brucite-hydromagnesite (5424). Although magnesite is the thermodynamically stable phase and, in conjunction with brucite, it would buffer f_{CO_2} at the lowest level among Mg carbonates, the formation of magnesite at ambient temperature is not favored kinetically. However, hydromagnesite (5424) is expected be converted to magnesite ($MgCO_3$) in the 10-ka period during which the repository is regulated by the EPA.

In Table 3, most of the calculations are based on the thermodynamic database of Königsberger et al. (1999) along with data from Cox et al. (1989). The f_{CO_2} for the two hydromagnesite varieties has been calculated by using the free energy of formation of brucite from Königsberger et al. (1999) and from Harvie et al. (1984). The f_{CO_2} differs by one order of magnitude when the different free energies of formation for brucite from these two sources are used. This indicates that there is a substantial discrepancy among the thermodynamic properties of brucite. Therefore, redetermination of its thermodynamic properties is desirable and has been summarized (Xiong, 2003); it will be published elsewhere.

3.5.4. Relative stability of hydromagnesite and nesquehonite

It is clear from the preceding discussion of f_{CO_2} that the relative stability of hydromagnesite (5424) and nesquehonite ($MgCO_3 \cdot 3H_2O$) at close to the room temperature is an important issue for nuclear waste isolation. In addition, during the weathering of terrestrial ultramafic/mafic rocks in northern

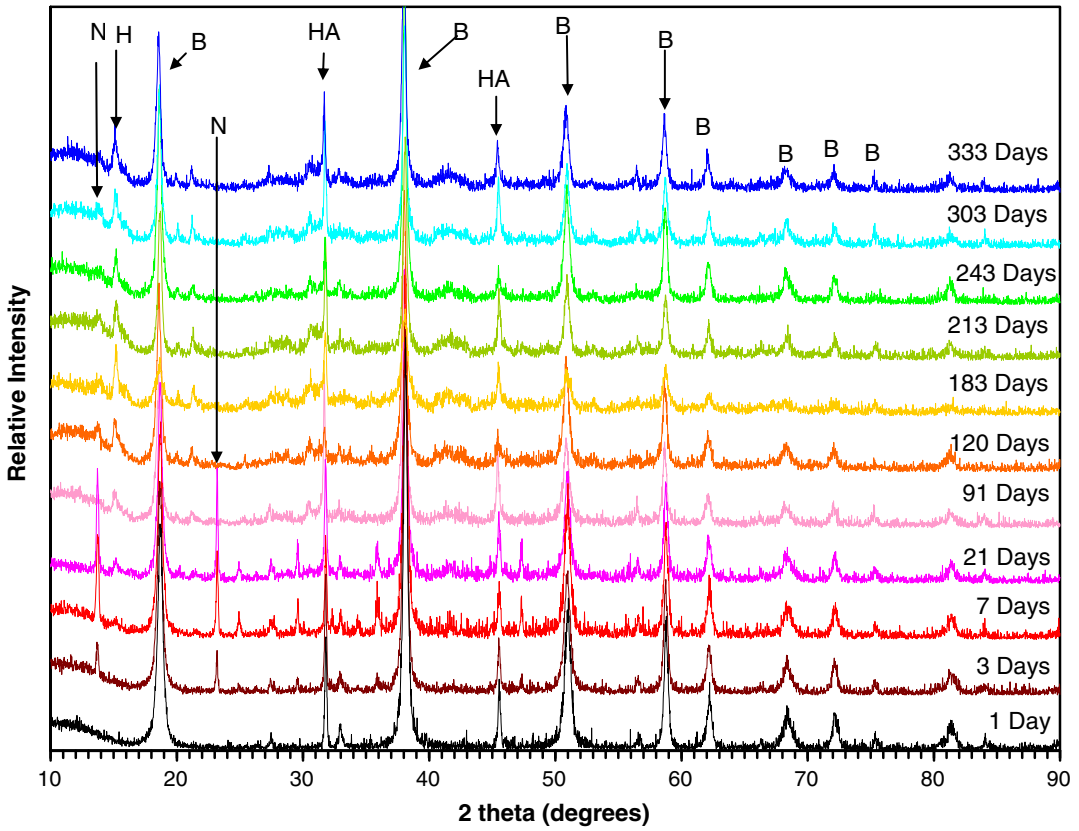

Fig. 15. XRD patterns for stirred experiments started with prehydrated *FMgO* at $P_{CO_2} = 5 \times 10^{-2}$ atm in ERDA-6. A mixture of 5 vol.% CO_2 with 95 vol.% N_2 gas was bubbled into the solution. Abbreviations are the same as those in Figs. 1–13.

British Columbia and Yukon Territory, and the terrestrial weathering of meteorites in the Antarctic, involving liquid water, the temperature could be as low as 5 °C (see the paragraphs below for details). Therefore, the relative stability between these two phases at temperatures as low as 5 °C is also important to our knowledge of weathering of ultramafic/mafic rocks in cold regions, and could have potential applications in the sequestration of anthropogenic CO_2.

The fugacity of CO_2 buffered by brucite-hydromagnesite (5424) differs from that buffered by brucite–nesquehonite by at least two orders of magnitude. Hydromagnesite (5424) is the predicted stable phase at ambient temperature and atmospheric CO_2 partial pressure ($P_{CO_2} = \sim 10^{-3.5}$ atm), and the predicted f_{CO_2} for the boundary between brucite and nesquehonite is $10^{-3.47}$ bars (Table 3), which is very close to atmospheric CO_2 partial pressure.

Previous studies regarding the relative stability of hydromagnesite and nesquehonite are not in total agreement, and do not provide clear boundary conditions for them. Lippmann (1973) stated that synthetic hydromagnesite and nesquehonite are in equilibrium, but the crystallization of the latter is delayed relative to the former by kinetic inhibitions because, if the hydromagnesite precipitate obtained at room temperature was left in contact with its mother liquid, nesquehonite was commonly found to have crystallized after some days. Lippmann (1973) synthesized hydromagnesite by mixing solutions of Mg (e.g., Mg chloride or sulfate) and alkali carbonates at concentrations such that precipitation occurred instantaneously. The temperature of the synthetic experiments was room temperature, but the intrinsic P_{CO_2} in the synthetic experiments is not known. In experiments conducted previously at Sandia National Laboratories at room temperature and $P_{CO_2} = 1$ atm, nesquehonite was formed (Zhang et al., 1999). Robie and Hemingway (1972) stated that nesquehonite is apparently unstable at room temperature and atmospheric CO_2, and nesquehonite starts to lose water and CO_2 after 3

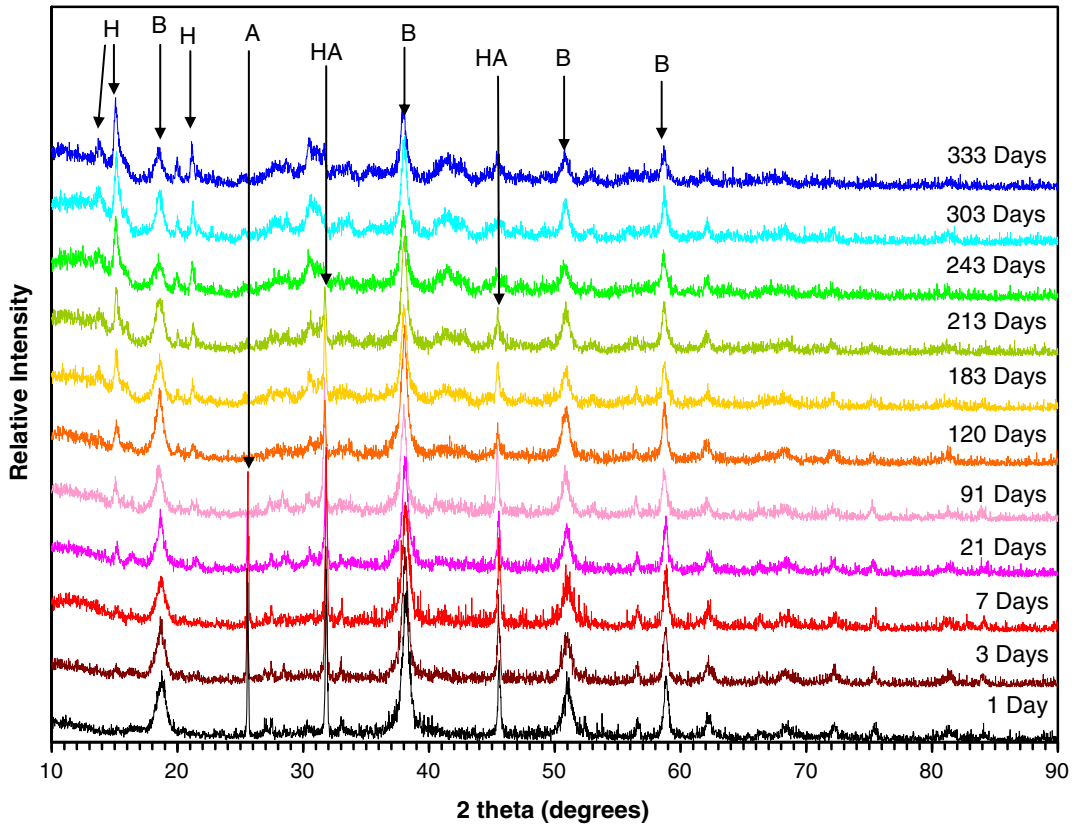

Fig. 16. XRD patterns for stirred experiments started with prehydrated *FMgO* at $P_{CO_2} = 5 \times 10^{-2}$ atm in GWB. A mixture of 5 vol.% CO_2 with 95 vol.% N_2 gas was bubbled into the solution. Abbreviation: A = anhydrite; other abbreviations are the same as those in Figs. 1 and 2.

weeks. In the tank experiments performed by Davies et al. (1977), using nesquehonite as starting material in the Port Alma brine from Queensland, Australia, nesquehonite was partially altered to hydromagnesite (variety unspecified) or protohydromagnesite after 10 days. After 130 days, strong XRD peaks of hydromagnesite developed, but nesquehonite was still present, though its peaks were weak.

The results from this study indicate that if the reaction path starts from the dissolution of brucite or periclase, or by extension, other Mg-bearing phases such as forsterite, at room temperature and atmospheric CO_2, nesquehonite will never form. This may be exemplified by the crystallization of hydromagnesite from fresh water seeping from the host rocks in basaltic caves in Kauai, Hawaii (Léveillé et al., 2000). This may also explain why hydromagnesite – not nesquehonite – exists in ore deposits in the Neraida area, south of Kozani, Greece (Arvanitidis, 1998), as this deposit is located in a Neogene sedimentary basin bounded by ultrabasic rocks (Arvanitidis, 1998). It can be envisioned that this hydromagnesite deposit was formed by solutions that were weathering ultrabasic rocks. As an analog, it is worth mentioning that hydromagnesite is observed in the Salt Lake (Tuz Golu) basin in central Anatolia, Turkey (Braithwaite and Zedef, 1994; Camur and Mutlu, 1996; Zedef et al., 2000). This basin is largely surrounded by mafic and ultramafic rocks (Camur and Mutlu, 1996; Zedef et al., 2000). In the Sabzevar ophiolite, the serpentine and the serpentinized harzburgite and dunite have been altered surficially to hydromagnesite (Shojaat et al., 2003).

At higher partial pressure of CO_2, i.e., $P_{CO_2} = 5 \times 10^{-2}$ atm in the present experiments, nesquehonite can be formed. This explains that successful synthesis of stable nesquehonite can take place only at P_{CO_2} higher than that of atmospheric CO_2 at room temperature, and usually at $P_{CO_2} = 1$ atm (Langmuir, 1965), well into its stability field. Therefore, the presence of nesquehonite at the Earth's surface should indicate high local partial

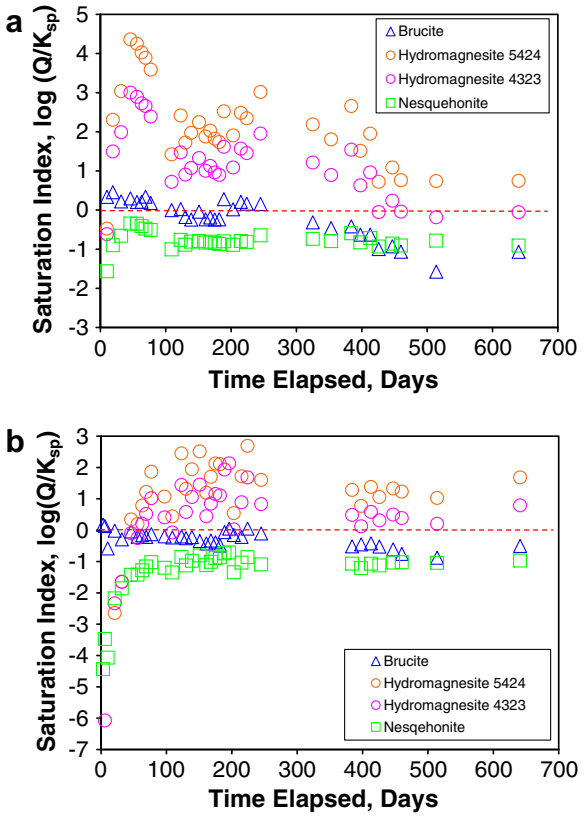

Fig. 17. Plots of saturation index versus run time for experiments using *FMgO* as starting material. (a) Run started with DI water. (b) Experiment started with 4.4 m NaCl solution.

pressure of CO_2 or temperatures (e.g., 5 °C) significantly lower than room temperature (see below for detailed explanations). For example, lichen weathering can create high local P_{CO_2} and nesquehonite has been observed to be associated with such lichen weathering (Gehrmann and Krumbein, 1994).

The observation that nesquehonite first appeared and then hydromagnesite (5424) subsequently formed in the experiments with ERDA-6 at $P_{CO_2} = 5 \times 10^{-2}$ atm might indicate that the conditions may be close to the boundary between hydromagnesite (5424) and nesquehonite. This could have important ramifications. The equilibrium between hydromagnesite (5424) and nesquehonite can be expressed as:

$$Mg_5(CO_3)_4(OH)_2 \cdot 4H_2O + CO_2(g) + 10H_2O = 5MgCO_3 \cdot 3H_2O \quad (8)$$

The equilibrium constant ($\log K_8$) at 25 °C for Reaction (8) calculated from the databases of Robie and Hemingway (1995) and Königsberger et al. (1999) are −2.05 and −2.01, respectively. The enthalpy change for Reaction (8) is −120 kJ mol^{-1} or −124 kJ mol^{-1} based on the data of Robie and Hemingway (1995) or Königsberger et al. (1999), respectively. The $\log K_8$ at 5 °C is calculated to be −0.55 or −0.44, respectively, by using the Van't Hoff equation. Accordingly, the relationship between the required activity of water and $\log f_{CO_2}$ can be expressed as:

$$\log\ a_{H_2O} = -\frac{\log\ K_8 + \log\ f_{CO_2}}{10} \quad (9)$$

In Table 4, the predicted log a_{H_2O} as a function of f_{CO_2} in a range from $10^{-3.5}$ to 10 bars are listed. From Table 4, it seems that both databases predict an unrealistic, minimum a_{H2O} (higher than 1.00) for the equilibrium between nesquehonite and hydromagnesite (5424) at 25 °C and 5 °C at f_{CO_2} up to 1.0 bars, implying that nesquehonite would never form at these temperatures even at $f_{CO_2} = 1.0$ bar. Apparently, neither database accommodates the co-existence of nesquehonite with hydromagnesite (5424) at atmospheric P_{CO_2} at ambient temperatures. Also these databases cannot explain the successful synthesis of nesquehonite in many experiments at room temperature and $P_{CO_2} = 1$ atm.

It should be mentioned that the above $\log K$ at 5 °C (278.15 K) calculated by using the Van't Hoff equation is satisfactory in comparison with the calculations using the following equation:

$$\Delta_r G^o_{278.15\ K} = \Delta_r H^o_{278.15\ K} - T\Delta_r S^o_{278.15\ K} \quad (10)$$

Assuming that the heat capacity change for Reaction (8) is constant over the temperature range from 25 °C to 5 °C, $\Delta_r H^o_{278.15\,K}$ and $\Delta_r S^o_{278.15\,K}$ are calculated from the following respective equations in their integrated forms:

$$(\partial \Delta_r H^o/\partial T)_p = \Delta_r C^o_p \quad (11)$$

$$(\partial \Delta_r S^o/\partial T)_p = \Delta_r C^o_p/T \quad (12)$$

In the calculations, the heat capacities of nesquehonite and hydromagnesite (5424) are from Robie and Hemingway (1972). In the database of Königsberger et al. (1999) these heat capacities are also from Robie and Hemingway (1972). The $\log K_8$ at 5 °C calculated from Eq. (10) are −0.45 and −0.47 for the databases of Robie and Hemingway (1995) and Königsberger et al. (1999), respectively. Therefore, the extrapolations by using the Van't Hoff equation differ from those calculated using Eq. (10) by only 0.1 log units at most in this temperature range.

In nature, both nesquehonite and hydromagnesite (5424) formed by terrestrial weathering have

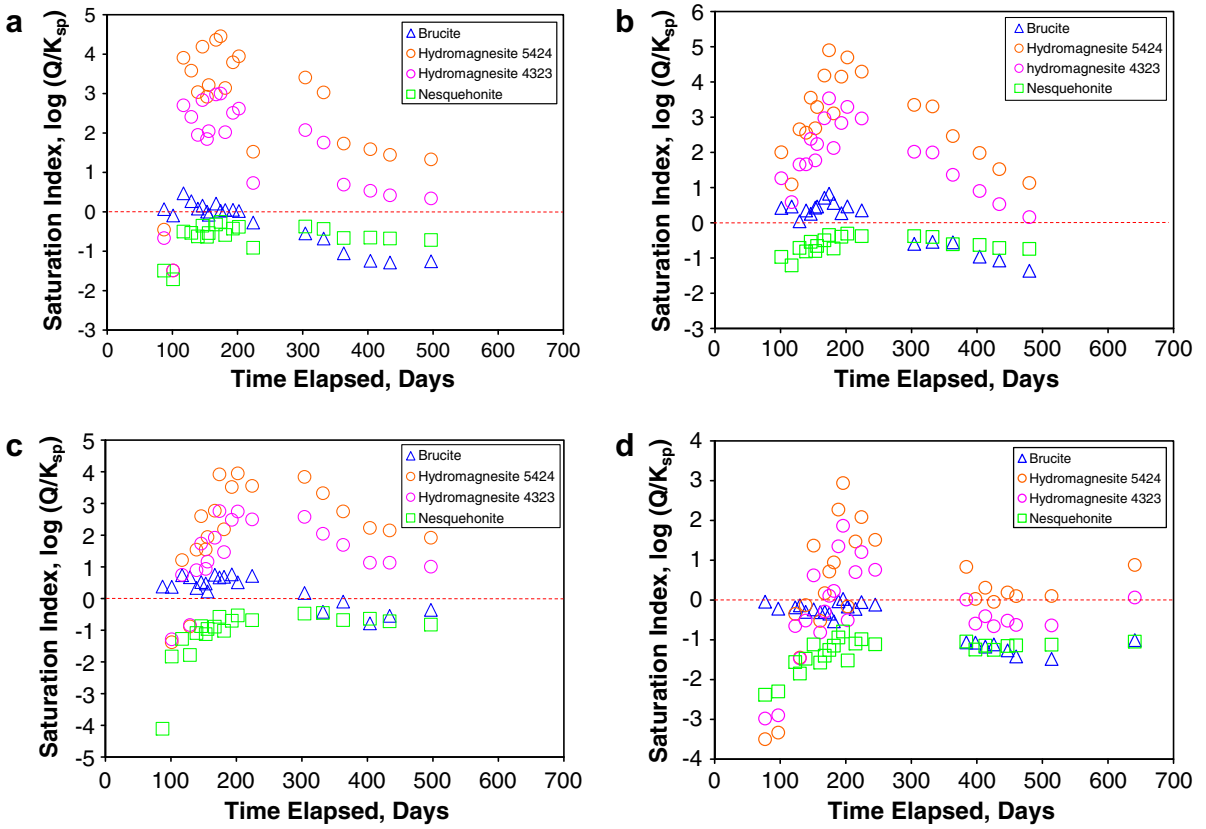

Fig. 18. Plots of saturation index versus run time for experiments using *PMgO*. (a) Run started with 0.010 m NaCl solution. (b) Run started with 0.10 m NaCl solution. (c) Run started with 1.0 m NaCl solution. (d) Run started with 4.4 m NaCl solution.

been observed on the ordinary chondrite LEW 85320 from the Antarctic (Gooding et al., 1988; Velbel et al., 1991). In addition, either nesquehonite or hydromagnesite, has also been observed in other meteorites from the Antarctic, including Yamato 74371, ALHA77231, ALHA77257 and ALHA77262 (Yabuki et al., 1976; Marvin, 1980; cited in Velbel et al., 1991). In serpentine-rich mine tailings, both nesquehonite and hydromagnesite (5424) have been observed at the surface of the tailings piles at the historical mine sites in Yukon Territory and northern British Columbia (Wilson et al., 2006). The temperature for terrestrial weathering of LEW 85320 involving liquid water is believed to have been around 5 °C (Velbel et al., 1991). The average temperature in Yukon Territory and northern British Columbia is certainly less than 25 °C. For instance, the average temperature in July is 14 °C and the temperature in winter ranges from 4 °C to −50 °C in Yukon Territory (Education Canada Network, 2007). The observation of both hydromagnesite (5424) and nesquehonite in these samples may indicate that the conditions (i.e., $P_{CO_2} = \sim 10^{-3.5}$ atm, and 25 °C < T ⩽ 5 °C) responsible for the weathering of ultramafic/mafic rocks involving liquid water may be close to the boundary between hydrogmagnesite (5424) and nesquehonite. However, according to the database of either Robie and Hemingway (1995) or Königsberger et al. (1999), at such P_{CO_2} and temperatures, the minimum activity of water required to stabilize nesquehonite is much higher than 1.00 (Table 4), which is unrealistic.

Based on the observation of nesquehonite and the subsequent appearance of hydromagnesite (5424) in the experiments with ERDA-6 at the laboratory room temperature and at $P_{CO_2} = 5\times 10^{-2}$ atm, $\log K_8$ is estimated to be ~2.5 at 25 °C in this study. In this estimation, $\log K_8$ at 25 °C is constrained by $\log a_{H_2O} = 0.748 \pm 0.001(2\sigma)$ calculated for ERDA-6 at that temperature (US DOE, 2004) and $f_{CO_2} = 5.07 \times 10^{-2}$ bars. In the estimation, $\log a_{H_2O}$ is rounded as 0.75. The $\log K_8$ at 5 °C is calculated to be ~4.0 by using the Van't Hoff

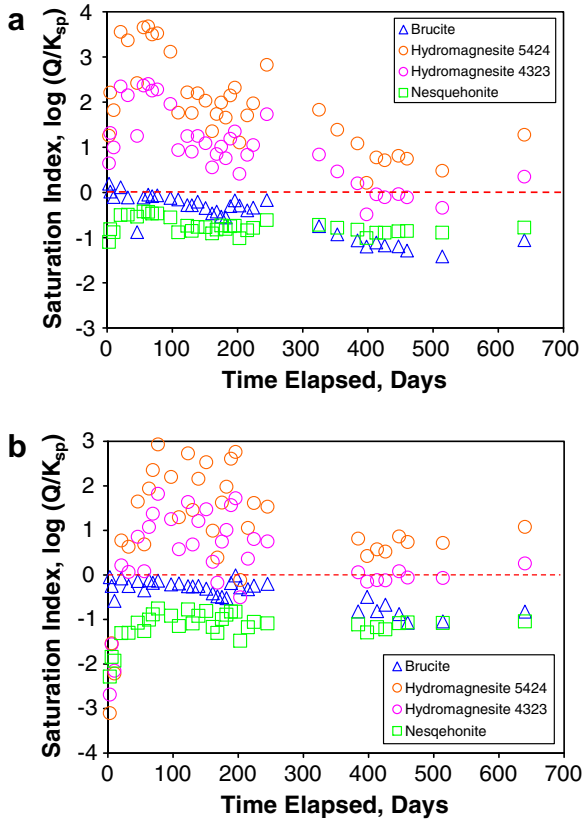

Fig. 19. Plots of saturation index versus run time for experiments using $FMg(OH)_2$ as starting material. (a) Run started with DI water. (b) Run started with 4.4 m NaCl solution.

equation with the enthalpy change from the database of Robie and Hemingway (1995).

Using the above $\log K_8$ estimated in this study, the predicted activity of water (Table 4) can adequately explain the above natural occurrences of hydromagnesite (5424) with nesquehonite, and the successful synthesis of nesquehonite at room temperature and $P_{CO_2} = 1$ atm in many studies. In addition, in the tank experiments of Davies et al. (1977), co-existence of hydromagnesite with nesquehonite is also observed. The intrinsic $\log f_{CO_2}$ and activity of water for the supernatant brine at 7.5 months of the tank experiments of Davies et al. (1977) is calculated to be −2.25 and 0.82, respectively, by using EQ3NR. As the temperatures of their experiments fluctuated between 10 °C and 28 °C, the above calculated intrinsic $\log f_{CO_2}$ and activity of water are in reasonable agreement with those values which predict the equilibrium between hydromagnesite (5424) and nesquehonite based on $\log K_8$ estimated by this study (Fig. 20).

In addition, the results from the experiments with GWB at room temperature and $P_{CO_2} = 5 \times 10^{-2}$ atm also support the estimated $\log K_8$ at 25 °C based on the experiments with ERDA-6. In the experiments with GWB at $P_{CO_2} = 5 \times 10^{-2}$ atm, nesquehonite is never observed. The activity of water for GWB at 25 °C is calculated to be $0.733 \pm 0.001(2\sigma)$ (US DOE, 2004). The minimum activity of water at 25 °C and $f_{CO_2} = 5.07 \times 10^{-2}$ bars ($5 \times 1.01325 \times 10^{-2}$ bars) for nesquehonite to be stable is calculated to be 0.76 (rounded from 0.7578) based on the $\log K_8$ at 25 °C. The fact that the calculated activity of water for GWB at 25 °C is lower than the required minimum activity of water for nesquehonite may well explain why nesquehonite is never observed in the experiments with GWB at $P_{CO_2} = 5 \times 10^{-2}$ atm (Fig. 20; also see XRD patterns in Figs. 14 and 16).

Mafic and ultramafic rocks have potential for sequestration of substantial amounts of anthropogenic CO_2 (e.g., McGrail et al., 2006). The atomic ratio of Mg to C is 1.25:1 and 1:1 in hydromagnesite (5424) and nesquehonite, respectively. Therefore, in order to be more efficient, sequestration of anthropogenic CO_2 is preferred under the conditions in the stability field of nesquehonite mentioned above.

Table 2
Calculated concentrations (in molality) of Mg^{2+}, OH^-, $CO_{2(aq)}$ and activity of H_2O, and measured concentration of H^+ as a function of ionic-strength

Experiment	Ionic-strength, m	Experimental time, d	$m_{Mg^{2+}}$	m_{H^+}	m_{OH^-}	m_{CO_2} (aq)	a_{H_2O}
PMgO–0.01Cl	0.010	404	5.23×10^{-3}	7.31×10^{-10}	1.94×10^{-5}	1.10×10^{-5}	0.9994
PMgO–0.1Cl	0.10	404	6.46×10^{-3}	5.13×10^{-10}	3.38×10^{-5}	6.67×10^{-6}	0.9963
PMgO–1.0Cl	1.0	404	1.12×10^{-2}	4.02×10^{-10}	4.78×10^{-5}	4.10×10^{-6}	0.9657
PMgO–4.0Cl	4.4	426	5.99×10^{-3}	2.43×10^{-10}	2.55×10^{-5}	1.69×10^{-6}	0.8343
FMgO–0Cl	0.0090	426	2.61×10^{-3}	4.14×10^{-10}	3.01×10^{-5}	3.29×10^{-6}	0.9998
FMgO–4.0Cl	4.4	426	6.34×10^{-3}	1.28×10^{-10}	4.87×10^{-5}	6.19×10^{-7}	0.8342
$FMg(OH)_2$–0Cl	0.010	426	3.12×10^{-3}	5.51×10^{-10}	2.30×10^{-5}	5.40×10^{-6}	0.9998
$FMg(OH)_2$–4.0Cl	4.4	426	5.77×10^{-3}	1.43×10^{-10}	4.34×10^{-5}	6.81×10^{-7}	0.8342

Table 3
Fugacity of CO_2 gas buffered by the assemblage of brucite and various magnesium carbonates at 25 °C

Buffer assemblage	Buffer reaction	$\log f_{CO_2}$	Sources of thermodynamic data[a]
Brucite–magnesite	$Mg(OH)_2(s) + CO_2(g) = MgCO_3(s, synthetic) + H_2O(l)$	−6.46	$\Delta_f G^o_{brucite}$[b]; $\Delta_f G^o_{magnesite}$[b]
	$Mg(OH)_2(s) + CO_2(g) = MgCO_3(s, natural) + H_2O(l)$	−7.09	$\Delta_f G^o_{brucite}$[b]; $\Delta_f G^o_{magnesite}$[b]
Brucite–hydromagnesite (5424)	$5Mg(OH)_2(s) + 4CO_2(g) = Mg_5(CO_3)_4(OH)_2 \cdot 4H_2O(s)$	−4.84	$\Delta_f G^o_{brucite}$[b]; $\Delta_f G^o_{hydromagnesite(5424)}$[b]
Brucite–hydromagnesite (5424)	$5Mg(OH)_2(s) + 4CO_2(g) = Mg_5(CO_3)_4(OH)_2 \cdot 4H_2O(s)$	−5.96	$\Delta_f G^o_{brucite}$[c]; $\Delta_f G^o_{hydromagnesite(5424)}$[b]
Brucite–hydromagnesite (4323)	$4Mg(OH)_2(s) + 3CO_2(g) = Mg_4(CO_3)_3(OH)_2 \cdot 3H_2O(s)$	−4.33	$\Delta_f G^o_{brucite}$[b]; $\Delta_f G^o_{hydromagnesite(4323)}$[d]
Brucite–hydromagnesite (4323)	$4Mg(OH)_2(s) + 3CO_2(g) = Mg_4(CO_3)_3(OH)_2 \cdot 3H_2O(s)$	−5.38	$\Delta_f G^o_{brucite}$[c]; $\Delta_f G^o_{hydromagnesite(4323)}$[d]
Brucite–nesquehonite	$Mg(OH)_2(s) + CO_2(g) + 2H_2O(l) = MgCO_3 \cdot 3H_2O(s)$	−3.47	$\Delta_f G^o_{brucite}$[b]; $\Delta_f G^o_{nesquehonite}$[b]
Brucite–artinite	$2Mg(OH)_2(s) + CO_2(g) + 2H_2O(l) = Mg_2(OH)_2CO_3 \cdot 3H_2O(s)$	−4.69	$\Delta_f G^o_{brucite_2}$; $\Delta_f G^o_{artinite}$[b]
Brucite–lansfordite	$Mg(OH)_2(s) + CO_2(g) + 4H_2O(l) = MgCO_3 \cdot 5H_2O(s)$	−3.22	$\Delta_f G^o_{brucite}$[b]; $\Delta_f G^o_{lansfordite}$[b]

[a] *Note*: In all calculations, thermodynamic data of CO_2(gas) and H_2O(l) are from CODATA (Cox et al., 1989) as this database is consistent with Königsberger et al. (1999), and the activity of water is assumed to be unity for reactions involving water.
[b] Königsberger et al. (1999).
[c] Harvie et al. (1984).
[d] Langmuir (1965).

Table 4
Predicted activity of water regarding equilibrium between hydromagnesite (5424) and nesquehonite represented by Reaction (8) as a function of $\log f_{CO_2}$ at 5 °C and 25 °C

	25 °C		5 °C		Remarks
$\log f_{CO_2}$	$\log a_{H_2O}$	a_{H_2O}	$\log a_{H_2O}$	a_{H_2O}	$\log K_8$ calculated from the database of Robie and Hemingway (1995)
−3.5	(5.55×10^{-1})[a]	(3.59)	(4.05×10^{-1})	(2.54)	
−3.0	(5.05×10^{-1})	(3.20)	(3.55×10^{-1})	(2.26)	
−2.5	(4.55×10^{-1})	(2.85)	(3.05×10^{-1})	(2.02)	
−2.0	(4.05×10^{-1})	(2.54)	(2.55×10^{-1})	(1.80)	
−1.5	(3.55×10^{-1})	(2.27)	(2.05×10^{-1})	(1.60)	
−1.0	(3.05×10^{-1})	(2.02)	(1.55×10^{-1})	(1.43)	
−0.5	(2.55×10^{-1})	(1.80)	(1.05×10^{-1})	(1.27)	
0	(2.05×10^{-1})	(1.60)	(5.46×10^{-2})	(1.13)	
0.5	(1.55×10^{-1})	(1.42)	4.60×10^{-3}	1.01	
1.0	(1.05×10^{-1})	(1.27)	-4.54×10^{-2}	0.901	
−3.5	(5.51×10^{-1})	(3.55)	(3.94×10^{-1})	(2.48)	$\log K_8$ calculated from the database of Königsberger et al. (1999)
−3.0	(5.01×10^{-1})	(3.16)	(3.44×10^{-1})	(2.21)	
−2.5	(4.51×10^{-1})	(2.82)	(2.94×10^{-1})	(1.97)	
−2.0	(4.01×10^{-1})	(2.52)	(2.44×10^{-1})	(1.76)	
−1.5	(3.51×10^{-1})	(2.24)	(1.94×10^{-1})	(1.56)	
−1.0	(3.01×10^{-1})	(2.00)	(1.44×10^{-1})	(1.39)	
−0.5	(2.51×10^{-1})	(1.78)	(9.44×10^{-2})	(1.24)	
0	(2.01×10^{-1})	(1.59)	(4.44×10^{-2})	(1.11)	
0.5	(1.51×10^{-1})	(1.41)	-5.58×10^{-3}	0.987	
1.0	(1.01×10^{-1})	(1.26)	-5.56×10^{-2}	0.880	
−3.5	(1.0×10^{-1})	(1.3)	-5.1×10^{-2}	0.89	$\log K_8$ estimated in this study. See text for details
−3.0	(5.0×10^{-2})	(1.1)	-1.0×10^{-1}	0.79	
−2.5	0	1.0	-1.5×10^{-1}	0.71	
−2.0	-5.0×10^{-2}	0.89	-2.0×10^{-1}	0.63	
−1.5	-1.0×10^{-1}	0.79	-2.5×10^{-1}	0.56	
−1.0	-1.5×10^{-1}	0.71	-3.0×10^{-1}	0.50	
−0.5	-2.0×10^{-1}	0.63	-3.5×10^{-1}	0.45	
0	-2.5×10^{-1}	0.56	-4.0×10^{-1}	0.40	
0.5	-3.0×10^{-1}	0.50	-4.5×10^{-1}	0.35	
1.0	-3.5×10^{-1}	0.45	-5.0×10^{-1}	0.32	

[a] Numbers in parentheses are unrealistic activity of water in logarithmic or linear scale.

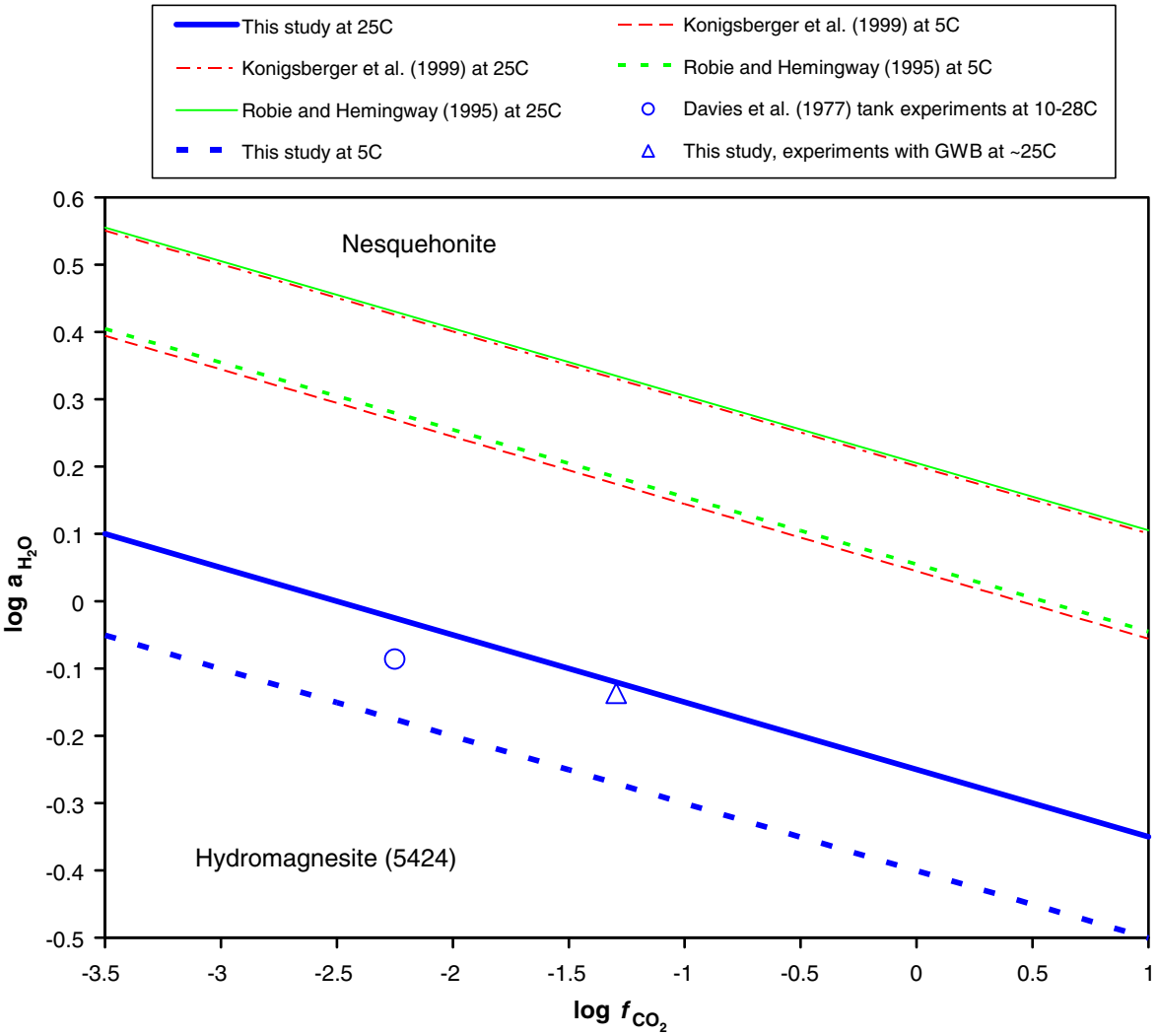

Fig. 20. Predicted boundaries between hydromagnesite (5424) and nesquehonite at 5 °C and 25 °C.

For example, the carbonation of forsterite (Mg_2SiO_4) as hydromagnesite (5424) and nesquehonite can be expressed as:

$$5Mg_2SiO_4 + 8CO_2(g) + 10H_2O(l) = 2Mg_5(CO_3)_4(OH)_2 \cdot 4H_2O + 5SiO_2(am) \quad (13)$$

$$Mg_2SiO_4 + 2CO_2(g) + 6H_2O(l) = 2MgCO_3 \cdot 3H_2O + SiO_2(am) \quad (14)$$

Accordingly, if anthropogenic CO_2 is sequestered as nesquehonite, 0.5 mol of forsterite can consume one mole of CO_2. In contrast, if CO_2 is sequestered as hydromagnesite (5424), 0.625 mol of forsterite are needed to consume 1 mol of CO_2. Therefore, the sequestration of anthropogenic CO_2 is optimal if the conditions of sequestration are maintained in the stability field of nesquehonite instead of that of hydromagnesite (5424).

Although the $\log K_8$ estimated in this study can adequately explain the co-existence of hydromagnesite (5424) and nesquehonite, it should be mentioned with a caveat that the $\log K_8$ proposed in this study is estimated from the experiments not specifically designed to explore the boundary between hydromagnesite (5424) and nesquehonite. Therefore, it is desirable to design experiments specifically for exploration of that boundary in future studies to confirm the present values.

3.5.5. Hydromagnesite(5424) versus nesquehonite as a precursor for dolomite

It has been suggested that hydromagnesite/nesquehonite and aragonite/calcite are likely to be the precursors for dolomite ($CaMg(CO_3)_2$) (Lippmann, 1973). Using aragonite as an example, the formation of dolomite can be expressed as:

$$Mg_5(CO_3)_4(OH)_2 \cdot 4H_2O + 5CaCO_3(\text{aragonite}) + CO_2(g) = 5CaMg(CO_3)_2(\text{dolomite}) + 5H_2O \quad (15)$$

$$MgCO_3 \cdot 3H_2O + CaCO_3(\text{aragonite}) = CaMg(CO_3)_2(\text{dolomite}) + 3H_2O \quad (16)$$

As this study demonstrates that nesquehonite does not form at the partial pressure of the atmospheric CO_2 and at room temperature, hydromagnesite (5424) should be the more likely precursor for dolomite. In addition, the preceding calculations indicate that hydromagnesite (5424) is more stable at higher temperatures, whereas nesquehonite is more stable at lower temperatures. When sediments are buried and are subject to diagenesis, temperatures are expected to increase. Therefore, nesquehonite would be further destabilized during diagenetic processes. Consequently, Reaction (15) would be more likely.

3.5.6. Possible martian metastable magnesium carbonates

It is also of interest to note that hydrous Mg carbonates such as hydromagnesite and artinite have been inferred to be present at the martian surface based upon the Mariner 6 and 7 infrared spectra and terrestrial telescopic spectra (Calvin et al., 1994; Bibring and Erard, 2001). Although the current P_{CO_2} at the surface of the Mars is about 6×10^{-3} atm (Bridges et al., 2001), it is inferred that the P_{CO_2} associated with the formation of secondary mineral assemblages in the Martian meteorite ALH 84001 was close to 5×10^{-2} atm (Bridges et al., 2001). Therefore, the experimental results at $P_{CO_2} = 5 \times 10^{-2}$ atm seem to support the interpretation of the existence of hydrous Mg carbonates (Calvin et al., 1994; Valley et al., 2007).

4. Summary

Based upon experimental results obtained from this study, the reaction path in the system of $MgO–CO_2–H_2O$ at ambient temperature in solutions with ionic-strength up to 7.1 M (8.3 m) can be summarized as follows.

At atmospheric CO_2, the reaction path in Na–Cl-dominated solutions with ionic strengths up to 5.8 m (including the experiments ranging from those started with DI water to those started in ERDA-6) is:

Periclase → brucite → hydromagnesite(5424)

At atmospheric CO_2, the reaction path in Mg–Na–Cl-dominated solutions such as GWB with an ionic-strength of 8.3 m is:

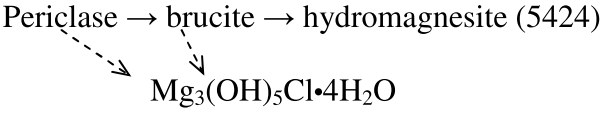

The dashed arrows above indicate that the addition of periclase or brucite to Mg–Na–Cl brines can result in the formation of $Mg_3(OH)_5Cl \cdot 4H_2O$ by raising the pH.

At $P_{CO_2} = 5 \times 10^{-2}$ atm, the reaction path in Na–Cl-dominated solutions (e.g., ERDA-6) is:

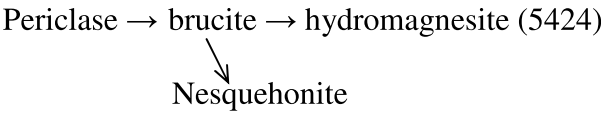

At $P_{CO_2} = 5 \times 10^{-2}$ atm, the reaction path in Mg–Na–Cl-dominated solutions (GWB) is

Periclase → brucite → hydromagnesite(5424)

As periclase or brucite is in excess relative to CO_2 produced by possible microbial activity in the WIPP, f_{CO_2} would be buffered by brucite and hydromagnesite (5424) according to the reaction paths demonstrated in this study.

Acknowledgements

Sandia National Laboratories is a multiprogram laboratory operated by Sandia Corporation, a Lockheed Martin Company, for the United States Department of Energy's National Nuclear Security Administration under Contract DE-AC04-94AL85000. This research is funded by WIPP programs administered by the Office of Environmental Management (EM) of the U.S Department of Energy. We wish to dedicate this work to Kelsey Mae Davis, who passed away on June 12, 2006, in

appreciation of her assistance. Our thanks are due to Nathalia Chadwick, Veronica Gonzales, and Shaundra Stone, for their laboratory assistance. Dr. Menghua Liu of University of Western Ontario, and an anonymous reviewer, are thanked for their insightful and thorough reviews. We wish to extend our thanks to Dr. Scott Wood for his comments on the manuscript. We also thank Dr. Ziya Cetiner for his editorial efforts.

Appendix A. Supplementary data

Supplementary data associated with this article can be found, in the online version, at doi:10.1016/j.apgeochem.2007.12.035.

References

Arvanitidis, N., 1998. Northern Greece's industrial minerals: production and environmental technology development. J. Geochem. Explor. 62, 217–227.

Bibring, J.-P., Erard, S., 2001. The Martian surface composition. Space Sci. Rev. 96, 293–316.

Bonatti, E., Ottonello, G., Hamlyn, P.R., 1986. Peridotites from island of Zabargad (St. John), Red Sea: petrology and geochemistry. J. Geophys. Res. 91 B1, 599–631.

Braithwaite, C.J.R., Zedef, V., 1994. Living hydromagnesite stromatolites from Turkey. Sed. Geol. 92, 1–5.

Bridges, J.C., Catling, D.C., Saxton, J.M., Swindle, T.D., Lyon, I.C., Grady, M.M., 2001. Alteration assemblages in martian meteorites: implications for near-surface processes. Space Sci. Rev. 96, 365–392.

Brush, L.H., 1990. Test Plan for Laboratory and Modeling Studies of Repository and Radionuclide Chemistry for the Waste Isolation Pilot Plant. SAND90-0266, Sandia National Laboratories, Albuquerque, NM. Available from the National Technical Information Service as DE90013595/XAB.

Bryan, C.R., Snider, A.C., 2001. MgO hydration and carbonation at Sandia National Laboratories Carlsbad Facility, Sandia National Laboratories Technical Baseline Reports, ERMS # 516749, p. 66–83 (Chapter 5).

Buick, I.S., Gibson, R.L., Cartwright, I., Maas, R., Wallmach, T., Uken, R., 2000. Fluid flow in metacarbonates associated with emplacement of the Bushveld Complex, South Africa. J. Geochem. Explor., 391–395.

Calvin, W.M., King, T.V.V., Clark, R.N., 1994. Hydrous carbonates on mars – evidence from mariner 6/7 infrared spectrometer and ground-based telescopic spectra. J. Geophys. Res. Planets 99, 14659–14675.

Camur, M.Z., Mutlu, H., 1996. Major-ion geochemistry and mineralogy of the Salt Lake (Tuz Gölü) basin, Turkey. Chem. Geol. 127, 313–329.

Cox, J.D., Wagman, D.D., Medvedev, V.A., 1989. CODATA Key Values for Thermodynamics. Hemisphere Publishing Corporation, New York.

Davies, P.J., Bubela, B., Ferguson, J., 1977. Simulation of carbonate diagenetic processes: formation of dolomite, huntite and monohydrocalcite by the reactions between nesquehonite and brine. Chem. Geol. 19, 187–214.

Deng, D.-H., Zhang, C.-M., 1999. The formation mechanism of the hydrate phases in magnesium oxychloride cement. Cement Concrete Res. 29, 1365–1371.

Education Canada Network, 2007. Canada Facts/Yukon. Web Address: <http://www.educationcanada.com/facts/index.phtml?sid=yk&a=1&lang=eng/>.

Gehrmann, D.K., Krumbein, E., 1994. Interactions between epilithic and endolithic lichens and carbonate rocks. In: Fassina, V.Ž., Ott, H., Zezza, F. (Eds.), The Conservation of Monuments in the Mediterranean Basin. Museum d'Histoire naturelle and Musee d'art et d'histoire, Ville de Geneve, pp. 311–316.

Gooding, J.L., Jull, A.J.T., Cheng, S., Velbel, M.A., 1988. Mg-carbonate weathering products in Antarctic meteorites: isotopic compositions and origin of nesquehonite from LEW85320. Lunar Planet. Sci. Conf. XIX, 397–398.

Grenthe, I., Fuger, J., Konings, R.J.M., Lemire, R.J., Muller, A.B., Nguyen-Trung, C., Wanner, H., 1992. Chemical Thermodynamics of Uranium. Elsevier Science Publishers, New York.

Harvie, C.E., Møller, N., Weare, J.H., 1984. The prediction of mineral solubilities in natural waters: the Na–K–Mg–Ca–H–Cl–SO_4–OH–HCO_3–CO_3–CO_2–H_2O system to high ionic strengths at 25 °C. Geochim. Cosmochim. Acta 48, 723–751.

Hinsinger, P., Plassard, C., Jaillard, B., 2006. Rhizosphere: a new frontier for soil biogeochemistry. J. Geochem. Explor. 88, 210–213.

Hostetler, P.B., Coleman, R.G., Evans, B.W., 1966. Brucite in Alpine serpentinites. Am Mineral. 51, 75–98.

Huot, F., Hebert, R., Varfalvy, V., Beaudoin, G., Wang, C.-S., Liu, Z.-F., Cotton, J., Dostal, J., 2002. The Beimarang me'lange (southern Tibet) brings additional constraints in assessing the origin, metamorphic evolution and obduction processes of the Yarlung Zangbo ophiolite. J. Asian Earth Sci. 21, 307–322.

Kennedy, G.C., 1956. The brucite-periclase equilibrium. Am. J. Sci. 254, 567–573.

Königsberger, E., Königsberger, L.C., Gamsjäger, H., 1999. Low-temperature thermodynamic model for the system Na_2CO_3–$MgCO_3$–$CaCO_3$–H_2O. Geochim. Cosmochim. Acta 63, 3105–3119.

Langmuir, D., 1965. Stability of carbonates in the system MgO–CO_2–H_2O. J. Geol. 73, 730–754.

Lemire, R.J., Fuger, J., Nitsche, H., Potter, P., Rand, M.H., Rydberg, J., Sphahiu, K., Sullivan, J.C., Ullman, W.J., Vitorge, P., Wanner, H., 2001. Chemical Thermodynamics of Neptunium and Plutonium. North-Holland, Amsterdam, The Netherlands.

Léveillé, R.J., Fyfe, W.S., Longstaffe, F.J., 2000. Unusual secondary Ca–Mg–carbonate–kerolite deposits in basaltic caves, Kauai, Hawaii. J. Geol. 108, 613–621.

Lippmann, F., 1973. Sedimentary Carbonate Minerals. Springer-Verlag, New York.

Marvin, U.B., 1980. Magnesium carbonate and magnesium sulfate deposits in Antarctic meteorites. Antarct. J. (US) 15, 54–55.

McGrail, B.P., Schaef, H.T., Ho, A.M., Chien, Y.J., Dooley, J.J., Davidson, C.L., 2006. Potential for carbon dioxide sequestration in flood basalts. J. Geophys. Res.-Solid Earth 111, B12201.

Munson, D.E., Jones, R.L., Hoag, D.L., Ball, J.R., 1987. Heated Axisymmetric Pillar Test (Room H): In Situ Data Report (February, 1985–April, 1987), Waste Isolation Pilot Plant (WIPP) Thermal/Structural Interactions Program. SAND87-2488. Sandia National Laboratories, Albuquerque, NM.

Neal, C., Stanger, G., 1984. Calcium and magnesium-hydroxide precipitation from alkaline groundwaters in Oman, and their significance to the process of serpentinization. Mineral. Mag. 48, 237–241.

Novak, C.F., 1996. Development of the FMT chemical transport simulator: coupling aqueous density and mineral volume fraction to phase composition. J. Contam. Hydrol. 21, 297–310.

Popielak, R.S., Beauheim, R.L., Black, S.R., Coons, W.E., Ellingson, C.T., Olsen, R.L., 1983. Brine Reservoirs in the Castile Formation, Waste Isolation Pilot Plant Project, Southeastern New Mexico. TME 3153. US Department of Energy WIPP Project Office, Carlsbad, NM.

Powers, D.W., Lambert, S.J., Shaffer, S.-E., Hill, L.R., Weart, W.D. (Eds.), 1976. Geological Characterization Report, Waste Isolation Pilot Plant (WIPP) Site, Southeastern New Mexico, vols. I and II. SAND 78-1596. Sandia National Laboratories, Albuquerque, NM.

Rai, D., Felmy, A.R., Juracich, S.I., Rao, F.F., 1995. Estimating the Hydrogen Ion Concentration in Concentrated NaCl and Na_2SO_4 Electrolytes. SAND94-1949. Sandia National Laboratories, Albuquerque, NM.

Robie, R.A., Hemingway, B.S., 1972. The heat capacities at low-temperatures and entropies at 298.15 K of nesquehonite, $MgCO_3 \cdot 3H_2O$, and hydromagnesite. Am. Mineral. 57, 1768–1781.

Robie, R.A., Hemingway, B.S., 1973. The enthalpies of formation of nesquehonite, $MgCO_3 \cdot 3H_2O$, and hydromagnesite, $5MgO \cdot 4CO_2 \cdot 5H_2O$. U.S. Geol. Surv. J. Res. 1, 543–547.

Robie, R.A., Hemingway, B.S., 1995. Thermodynamic properties of minerals and related substances at 298.15 K and 1 bar (10^5 pascals) pressure and at higher temperatures. U.S. Geol. Surv. Bull., 2131.

Schuessler, W., Metz, V., Kienzler, B., Vejmelka, P., 2002. Geochemically based source term assessment for the Asse salt mine: comparison of modeling and experimental results (abstract). In: Prog. Abstr. Materials Research Soc. Annual Meeting at Boston, MA, p. 713.

Sciuto, P.F., Ottonello, G., 1995. Water-rock interactions on Zabargad Island, Red Sea-A case study. I. Applications of the concept of local equilibrium. Geochim. Cosmochim. Acta 59, 2187–2206.

Shojaat, B., Hassanipak, A.A., Mobasher, K., Ghazi, A.M., 2003. Petrology, geochemistry and tectonics of the Sabzevar ophiolite, north central Iran. J. Asian Earth Sci. 21, 1053–1067.

Silva, R.J., Bidoglio, G., Rand, M.H., Robouch, P.B., Wanner, H., Puigdomenech, I., 1995. Chemical Thermodynamics of Americium. North-Holland, Amsterdam, The Netherlands.

Stein, C.L., 1985. Mineralogy in the Waste Isolation Pilot Plant (WIPP) Facility Stratigraphic Horizon. Sandia National Laboratories Report, SAND85-0321. Available from the National Technical Information Service as DE8600571.

Swift, P.N., Corbet, T.F., 2000. The geologic and hydrogeologic setting of the Waste Isolation Pilot Plant. Reliab. Eng. Syst. Safety 69, 47–58.

US DOE, 1996. Title 40 CFR Part 191 Compliance Certification Application. Appendix SOTERM. DOE/CAO 1996-2184. US DOE Carlsbad Area Office, Carlsbad, NM.

US DOE, 2004. Title 40 CFR Part 191 Compliance Recertification Application for the Waste Isolation Pilot Plant, vol. 1-8. DOE/WIPP 2004-3231. US DOE Carlsbad Field Office, Carlsbad, NM.

Valley, J.W., Ushikubo, T., Kita, N.T., 2007. In situ analysis of three oxygen isotopes and OH in ALH 84001: further evidence of two generations of carbonates. Lunar and Planetary Science Conf. XXXVIII, Abstract #1147.

Velbel, M.A., Long, D.T., Gooding, J.L., 1991. Terrestrial weathering of Antarctic stone meteorites: formation of Mg-carbonates on ordinary chondrites. Geochim. Cosmochim. Acta 55, 67–76.

Wicks, F.J., Whittaker, E.J.W., 1977. Serpentine textures and serpentinization. Can. Mineral. 15, 459–488.

Wilson, S.A., Raudsepp, M., Dipple, G.M., 2006. Verifying and quantifying carbon fixation in minerals from serpentine-rich mine tailings using the Rietveld method with X-ray powder diffraction data. Am. Mineral. 91, 1331–1341.

Wolery, T.J., 1992a. EQ3/6, A Software Package for Geochemical Modeling of Aqueous Systems: Package Overview and Installation Guide (Version 7.0). UCRL-MA-110662 PT I. Lawrence Livermore National Laboratory, Livermore, CA.

Wolery, T.J., 1992b. EQ3NR, A Computer Program for Geochemical Aqueous SpeciationSolubility Calculations: Theoretical Manual, User's Guide, and Related Documentation (Version 7.0). UCRL-MA-110662 PT III. Lawrence Livermore National Laboratory, Livermore, CA.

Xiong, Y.-L., 2003. Revised thermodynamic properties of brucite determined by solubility studies and its significance to nuclear waste isolation. Geol. Soc. Am. Ann. Meet., Abstr. Prog. 34 (7), 102–103.

Xiong, Y.-L., Snider, A.C., 2003. 4.3 Carbonation Rates of the Magnesium Oxide Hydration Product Brucite in Various Solutions, Sandia National Laboratories Technical Baseline Reports, p. 4.3-1–4.3-11, WBS 1.3.5.3, Compliance Monitoring; WBS 1.3.5.4, Repository Investigations, Milestone RI 03-210, January 31, 2003. Sandia National Laboratories. ERMS 526049, Carlsbad, NM.

Yabuki, H., Okada, H., Shima , M., 1976. Nesquehonite found on the Yamato 74371 meteorite. Scientific Papers of Institute of Physics and Chemistry Research 70, 22–29.

Zedef, V., Russell, M.J., Fallick, A.E., Hall, A.J., 2000. Genesis of vein stockwork and sedimentary magnesite and hydromagnesite deposits in the ultramafic terranes of southwestern Turkey: a stable isotope study. Econ. Geol. 95, 429–445.

Zhang, P.-C., Anderson Jr., H.L., Papenguth, H.W., Krumhansl, J.L., 1999. Behavior of MgO Backfill as a CO_2 Scavenger at the Waste Isolation Pilot Plant (WIPP), Carlsbad, New Mexico (abstract). Materials Research Soc., Fall Meeting, Boston, MA.

Zhang, Z.-Y., Dai, C.-L., Zhang, Q.-C., Guo, B.-Z., Liu, W.-L., 1991. Formation mechanism on phase-5 and phase-3. Sci. China Ser. B 34, 1501–1509.

Zhao, Y.-M., Zhang, Y.-N., Bi, C.-S., 1999. Geology of gold-bearing skarn deposits in the middle and lower Yangtze River Valley and adjacent regions. Ore Geol. Rev. 14, 227–249.